

The Frequency-Domain Lattice Boltzmann Method (FreqD-LBM): A Versatile Tool to Predict the QCM Response Induced by Structured Samples

Diethelm Johannsmann,* Paul Häusner, Arne Langhoff, Christian Leppin, Ilya Reviakine, and Viktor Vanoppen

The quartz crystal microbalance with dissipation monitoring (QCM-D) is routinely used to investigate structured samples. Here, a simulation technique is described, that predicts the shifts of frequency and half bandwidth, Δf_n and $\Delta \Gamma_n$, of a quartz resonator operating on different overtone orders, n , induced by structured samples in contact with the resonator surface in liquid. The technique, abbreviated as FreqD-LBM, solves the Stokes equation in the frequency domain. The solution provides the complex amplitude of the area-averaged tangential stress at the resonator surface, from which Δf_n and $\Delta \Gamma_n$ are derived. Because the dynamical variables are complex amplitudes, the viscosity can be complex, as well. The technique naturally covers viscoelasticity. Limitations are linked to the grid resolution and to problems at large viscosity. Validation steps include viscoelastic films, rough surfaces, an oscillating cylinder in a viscous medium, and a free-floating sphere above the resonator. Application examples are soft adsorbed particles, stiff adsorbed particles, and a large, immobile spherical cap above the resonator, which allows to study the high-frequency properties of the material in the gap. FreqDLBM runs on an office PC and does not require expert knowledge of numerical techniques. It is accessible to an experimentalist.

frequencies in the MHz range.^[1] The electronics interrogates the shifts of the resonance frequency, Δf_n , and of the half bandwidth, $\Delta \Gamma_n$, induced by the contact with a sample. It does so on a few different overtones, where overtones are typically labeled by the overtone order, n (often $n = 3, 5, 7, 9$ leading to frequencies of 15, 25, 35, and 45 MHz if the frequency of the fundamental is $f_0 = 5$ MHz). The half bandwidth will be called bandwidth for brevity in the following. $\Delta \Gamma$ and the shift in the “dissipation factor” (“ ΔD ”) are related as $\Delta D = 2\Delta \Gamma / f_{\text{res}}$. The terms “bandwidth” and “dissipation” can be used interchangeably. The dissipation here is synonymous to the inverse Q-factor. The *half* bandwidth is used rather than the full width at half maximum (FWHM), because the shifts in the half bandwidth can be viewed as the imaginary part of a complex frequency shift (if the resonances are sharp).^[2]

The parallel-plate model describes the vibration modes of the QCM reasonably well.^[2] Within this model, the displacement


of the top surface of the resonator occurs along the x-direction and has the same amplitude everywhere. The amplitude distribution is ignored (even though it does exist in practice). The value of the amplitude (usually < 1 nm) is irrelevant as long as it is small

1. Background and Scope

The quartz crystal microbalance with dissipation monitoring (QCM-D, QCM for short) is an acoustic resonator with

D. Johannsmann, A. Langhoff, C. Leppin
Institute of Physical Chemistry
Clausthal University of Technology
D38678 Clausthal-Zellerfeld, Germany
E-mail: johannsmann@pc.tu-clausthal.de

P. Häusner
Department of Information Technology
Uppsala University
Lägerhyddsvägen 1, Uppsala S-75237, Sweden

 The ORCID identification number(s) for the author(s) of this article can be found under <https://doi.org/10.1002/adts.202401373>

© 2025 The Author(s). Advanced Theory and Simulations published by Wiley-VCH GmbH. This is an open access article under the terms of the [Creative Commons Attribution](https://creativecommons.org/licenses/by/4.0/) License, which permits use, distribution and reproduction in any medium, provided the original work is properly cited.

DOI: 10.1002/adts.202401373

C. Leppin
Analytical Chemistry II – Shape-dependent Electrochemistry
Ruhr-University Bochum
Universitätsstr. 150, D-44801 Bochum, Germany

I. Reviakine
Advanced Wave Sensors S.L.
Táctica Business Park, Algepsers street, 24-1, Paterna 46988, Valencia, Spain

I. Reviakine
Department of Bioengineering
University of Washington
Seattle, WA 98195, USA

V. Vanoppen
Department of Chemistry
Angstrom Laboratory
Uppsala University
Lägerhyddsvägen 1, Uppsala S-75237, Sweden

enough to let the stress-displacement relation be linear. This is realistic in most QCM experiments (section 3.1). In all cases considered here, the reference state is the resonator immersed in a semi-infinite Newtonian liquid (solvent or buffer).^[3,4] All shifts of the resonance parameters are referenced to this state.

The simplest samples consist of thin, stiff, planar layers. These lead to “Sauerbrey behavior”.^[5] The Sauerbrey equation predicts

$$\frac{\Delta f_n}{n} = \frac{2f_0^2}{Z_q} \Delta m = \frac{2f_0^2}{Z_q} \rho_{\text{film}} d_{\text{Sau}} \quad (1)$$

$$\frac{\Delta \Gamma_n}{n} = 0$$

$Z_q = 8.8 \cdot 10^6 \text{ kg m}^{-2} \text{ s}^{-1}$ is the shear wave impedance of the resonator plate. It is a materials parameter, pertaining to the quartz plate. Δm is the mass per unit area of the sample, ρ_{film} is the film’s density, and d_{Sau} is the layer thickness. If ρ_{film} is known (it often is), the film thickness, d_{Sau} , can be derived from the frequency shift. d_{Sau} as derived from Equation (1) may be an apparent thickness, as indicated by the subscript “Sau”. For 5 MHz crystals and $\rho_{\text{film}} = 1 \text{ g cm}^{-3}$, a film with a thickness of 1 nm lowers the frequency of the fundamental by 5.8 Hz (meaning that $\Delta f_n/n \approx -5.8 \text{ Hz}$ on all overtones). For samples in air, the Sauerbrey equation follows from all stresses being caused by inertia. It then is based on inertia, only, and applies in an average sense ($\Delta m \rightarrow \langle \Delta m \rangle_{\text{area}}$). In liquids, the Sauerbrey equation is less fundamental. It is the result of a first-order Taylor expansion in film thickness of a more general equation, and it only applies to planar layers. An apparent thickness of this kind can also be derived from the frequency shifts induced by structured samples. However, structured adsorbates often look like moderately soft films to the QCM. Ref. [6] discusses one of many examples. The apparent softness arises from the motion of the adsorbates around the contact point. As shown in section 7.1, this aspect is captured by the FreqD-LBM method.

In the Sauerbrey limit, the overtone-normalized frequency shifts are the same on all overtones ($\Delta f_n/n \approx \text{const.}$), and the shifts in half bandwidth are much smaller than the negative frequency shifts ($\Delta \Gamma_n/n \ll -\Delta f_n/n$). If Equation (1) holds (or if it approximately holds), the QCM operates in the “gravimetric” regime. In the following, the interest is in non-gravimetric effects. Because these are discussed against the background of gravimetry, it is customary to replace Δf_n and $\Delta \Gamma_n$ by the overtone-normalized shifts of frequency and bandwidth, $\Delta f_n/n$ and $\Delta \Gamma_n/n$. Those appear on the left-hand side of Equation (1). Typical indicators of non-gravimetric behavior are $\Delta \Gamma_n/n > 0$ and $\Delta f_n/n$ increasing with overtone order.

For planar samples, a viscoelastic model exists, which predicts $\Delta f_n/n$ and $\Delta \Gamma_n/n$ from the geometric parameters and the viscoelastic constants.^[2] By fitting this model to the data, viscoelastic parameters (such as the shear modulus and its frequency dependence) can be derived from the sets of $\Delta f_n/n$ and $\Delta \Gamma_n/n$. The standard errors from the fit can be substantial, though.^[7]

As the areas of application of the QCM expand,^[8] structured samples are studied more and more often. Classic examples are liposomes in liquid, which first adsorb in roughly spherical shape and later rupture to form flat supported lipid bilayers (SLBs).^[9] The spherical adsorbates increase the bandwidth, but the band-

width returns to its original value once the SLBs have developed. While this picture matches intuition, quantitative modeling would be desirable. Other cases, that would benefit from such quantitative models, include adsorbed particles^[10,11] and rough surfaces.^[12]

There is a canonical way to formulate such models. The equations of hydrodynamics and viscoelasticity must be solved for a given geometry, a given set of viscoelastic constants, and a given set of boundary conditions. The solution will amount to an oscillatory flow field. The oscillatory flow will induce an oscillatory stress at the resonator surface. Following the small-load approximation,^[2] $\Delta f_n/n$ and $\Delta \Gamma_n/n$ are proportional to the imaginary and the real part of the area-averaged complex amplitude of this transverse stress, $\langle \tilde{\sigma}^S \rangle_{\text{area}}$. The superscript S denotes the substrate. The transverse stress is the xy-component of the stress tensor with x the direction of the oscillatory displacement and y the surface normal. The transverse stress at $y = 0$ follows straightforwardly from the oscillatory flow field (the latter being a field of complex amplitudes). When $\Delta f_n/n$ and $\Delta \Gamma_n/n$ are subsumed under a complex frequency shift, $\tilde{\Delta f}_n/n = \Delta f_n/n + i\Delta \Gamma_n/n$,^[13] the small-load approximation states that

$$\frac{\tilde{\Delta f}_n}{n} = \frac{\Delta f_n + i\Delta \Gamma_n}{n} = \frac{\Delta f_n + i(f_{\text{res}} \Delta D_n/2)}{n} \approx \frac{if_0}{n\pi Z_q} \langle \tilde{Z}_L \rangle_{\text{area}}$$

$$= \frac{if_0}{n\pi Z_q} \frac{\langle \tilde{\sigma}^S \rangle_{\text{area}}}{\tilde{u}_x^S} \quad (2)$$

The tilde (\sim) denotes complex parameters. (The tilde will be omitted later for notational brevity.) Both $\tilde{\sigma}^S$ and \tilde{u}_x^S are complex amplitudes. The ratio of the two is the load impedance, \tilde{Z}_L . \tilde{u}_x^S , which is the transverse velocity of the resonator surface, can be chosen as unity everywhere on the surface (a boundary condition). When in contact with either a soft sample or a thin sample, the QCM is under strain control. The QCM prescribes the motion of the resonator surface and measures the small stress (indirectly, via the complex frequency shift). This is the essence of the small-load approximation.

All such models require hypotheses entailing sample geometry and viscoelastic constants. They generate complex frequency shifts, $\{(\tilde{\Delta f}_n/n)_{\text{model}}\}$, that can be compared with the experimental results, $\{(\tilde{\Delta f}_n/n)_{\text{expt}}\}$. If the hypothesis contains free parameters, these may be determined from the comparison. The simulations only run forward. They cannot directly determine the geometry and viscoelastic parameters from a set of experimental observations, $\{(\tilde{\Delta f}_n/n)_{\text{expt}}\}$, because this problem is underdetermined. Part of the challenge is to condense the problem under study into a sufficiently simple set of parameters, which can be derived from the comparison between $\{(\tilde{\Delta f}_n/n)_{\text{model}}\}$ and $\{(\tilde{\Delta f}_n/n)_{\text{expt}}\}$.

The calculation of the flow field in three dimensions presents a challenge. In principle, any of the methods of computational fluid dynamics can be used to calculate this field. Indeed, the first author’s group has in the past employed the finite element method (FEM), using COMSOL.^[14] This work demonstrated the principles, but only produced robust results in 2D. What looked like spheres in the sketches, were actually cylinders. Xie et al. have computed $\Delta f_n/n$ and $\Delta \Gamma_n/n$ as induced by the contact with a particle in air.^[15] The dry environment avoided the complications

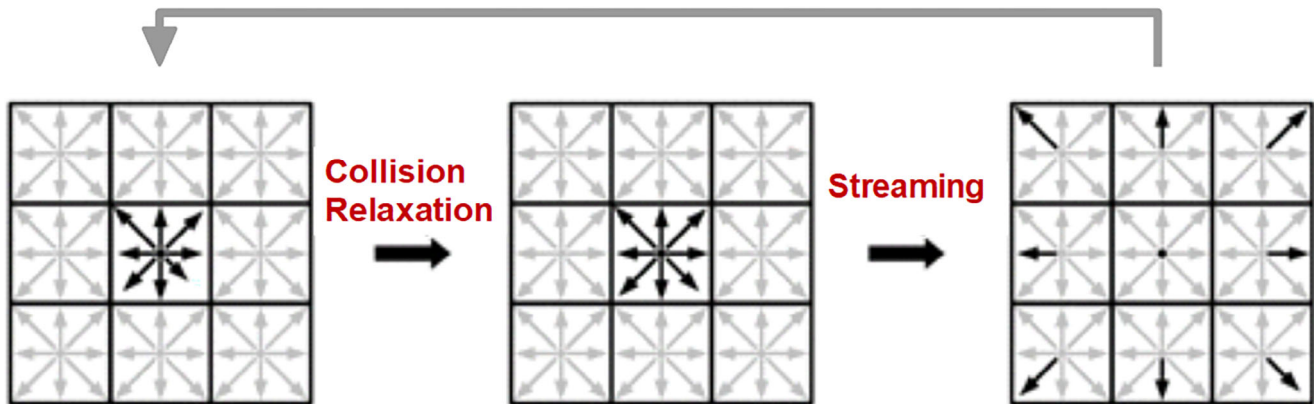


Figure 1. Illustration of the lattice Boltzmann algorithm in 2D, using the D2Q9 stencil. In the collision step (which often amounts to a relaxation), the populations on the nodes are updated following certain rules. In the streaming step, the populations are transported along their respective lattice velocities, c_i , to the neighboring nodes. Adapted from ref. [21].

inherent to the boundary conditions. The particle in air could be modeled in 3D with FEM.

Delgado-Buscalioni and coworkers have recently modeled QCM problems with the immersed boundary method.^[16,17] The calculation is an add-on to the package FLUAM,^[18] which today is part of another package, namely UAMMD. The calculations were done at a high-performance computing facility. They require expertise with these methods. It may be assumed that the method is powerful and can solve problems, which are more complicated than the problems amenable to FreqD-LBM.

Gillissen and coworkers have applied conventional LBM to QCM problems.^[19,20] These calculations were computationally expensive and required a rather coarse grid, in consequence. The calculation confirmed what is predicted by the “extrapolation scheme” (section 7.1).

The method described herein, FreqD-LBM, is a variant of LBM, which – applied to QCM problems – is more efficient than conventional LBM. (FreqD stands for “frequency domain”.) FreqD-LBM is much simpler than the algorithm put forward by Delgado-Buscalioni.^[16,17] Compared to standard LBM, a distinct advantage of FreqD-LBM is that the domain boundaries remain fixed in space. The movement is taken care of by the oscillation amplitudes. The core of the code fits into a few dozen lines. By far the largest part of the code handles pre-processing and post-processing. Of course, some basic understanding of the lattice Boltzmann method is needed. LBM is, for instance, comprehensively described in ref. [22]. Ref. [22] is the source most often quoted for technicalities here.

LBM employs a grid in space, a fixed time step, and a fixed set of velocities (Figure 2). The state of the system is encoded in populations on the nodes, f_i , having one of the velocities. The populations evolve by an alternation of “collision” and “streaming” (Figure 1). (“Collision” is synonymous to “relaxation” in this text.) That such a simple algorithm should be as successful as it actually is, comes as a surprise to the non-expert. There is a price to be paid: LBM is not very flexible. Ref. [22] expresses this as follows: “The beauty, yet weakness, of the LBE [of the lattice Boltzmann equation] lies in its explicitness and uniform grid.” The mesh is not easily adapted to complicated geometries. LBM deteriorates in accuracy when the parameters leave the preferred

range. There are a few systematic errors, which are not easily corrected for. Among the advantages of LBM is that parallelization is rather easy because the collision step is local and can be distributed to different processors. Parallelization at this level has not yet been carried out for FreqD-LBM.

The algorithm underlying FreqDLBM was originally proposed by Shi and Sader.^[23] The goal mostly was the calculation of the resonance frequencies and resonance bandwidths of nanoresonators (such as AFM cantilevers) in liquids. The medium was a homogeneous Newtonian liquid. Vigen has also reported on the application of lattice Boltzmann method to acoustics.^[24,25] He employs similar amplitudes as FreqD-LBM, but his treatment differs from the Shi-Sader model (see section 3.2).

Ref. [23] contains mathematical background, which includes a treatment in the framework of the Chapman-Enskog theory. As discussed in section 6.2, FreqD-LBM as used here slightly differs from the Shi-Sader model. We test for its correctness using the dispersion relation (the k - ω relation) for plane shear waves. This test is less general than the full Chapman-Enskog analysis. For this special test, we find “second order accuracy” if the quadratic term in the relaxation step is of the form $+5/2 \omega^2 h^{\text{eq}}$ rather than $-1/2 \omega^2 h^{\text{eq}}$ as proposed in ref. [23]. Second order accuracy was tested based on the complex frequency shift induced by a semi-infinite Newtonian liquid.

In FreqD-LBM, the populations are replaced by complex amplitudes, h_i . The amplitudes are assumed to be so small that the flow field obeys a linearized theory. The absolute amplitude then cannot be used to convert between lattice units and real-world units because it can take any value. The oscillatory nature of movement is accounted for by adding the term $-i\omega h$ in the collision step. FreqD-LBM solves the Stokes equation in the frequency domain (Equation 6). From the solution of the Stokes equation, one infers the oscillatory stress at the resonator surface, which is converted to $(\Delta \tilde{f}_n/n)_{\text{model}}$ with Equation (2). The properties of the sample are encoded in the complex kinematic viscosities on the nodes, $\nu(\mathbf{r})$. (This concerns soft samples. For rigid particles, see section 2.5.)

The appendix, which describes a boundary condition at the top based on a Fourier decomposition of the flow field, stands somewhat separately from the rest of the text. The analytical solution of

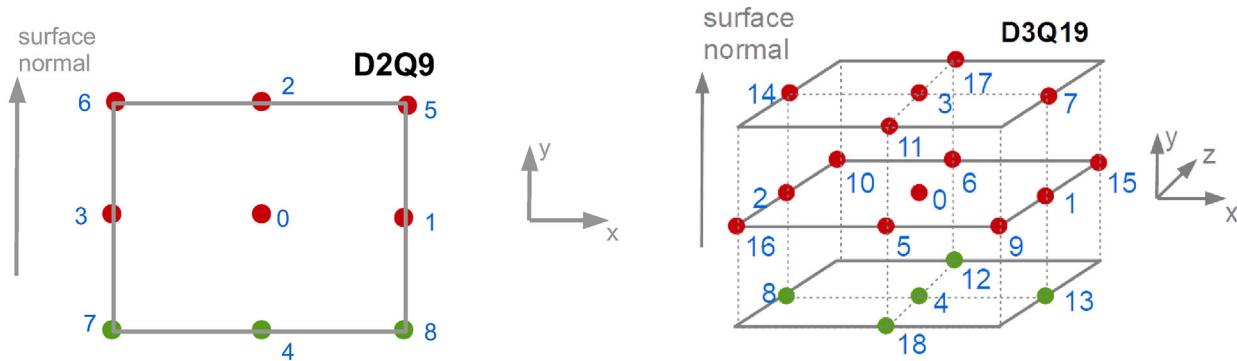


Figure 2. Discrete velocities in the D2Q9 and in the D3Q19 stencil (adapted from ref. [22]). In the D2Q9 stencil, the weight parameters are $\{w_i\} = 4/9, 1/9, 1/9, 1/9, 1/9, 1/36, 1/36, 1/36, 1/36$. The reversed directions needed in bounce-back are $\bar{i}(i) = 0 \rightarrow 0, 1 \rightarrow 3, 2 \rightarrow 4, 3 \rightarrow 1, 4 \rightarrow 2, 5 \rightarrow 7, 6 \rightarrow 8, 7 \rightarrow 5, \text{ and } 8 \rightarrow 6$. In the D3Q19 stencil, the weight parameters are $\{w_i\} = 1/3, 1/18, 1/18, 1/18, 1/18, 1/18, 1/18, 1/36, 1/36, 1/36, 1/36, 1/36, 1/36, 1/36, 1/36, 1/36, 1/36, 1/36$. The reversed directions are $\bar{i}(i) = 0 \rightarrow 0, 1 \rightarrow 2, 2 \rightarrow 1, 3 \rightarrow 4, 4 \rightarrow 3, 5 \rightarrow 6, 6 \rightarrow 5, 7 \rightarrow 8, 8 \rightarrow 7, 9 \rightarrow 10, 10 \rightarrow 9, 11 \rightarrow 12, 12 \rightarrow 11, 13 \rightarrow 14, 14 \rightarrow 13, 15 \rightarrow 16, 16 \rightarrow 15, 17 \rightarrow 18, \text{ and } 18 \rightarrow 17$.

the hydrodynamics problem in the bulk has little to do with LBM. The resulting set of equations can also be of benefit to other numerical packages. This might include the work reported in refs. [16] and [17].

An early version of FreqD-LBM was described in ref. [27]. More recent work is contained in refs. [28] and [29]. The technique has matured and the code was uploaded to Github. This text describes FreqD-LBM comprehensively. It should enable researchers to adapt the formalism to their problems.

A word of modesty: The authors are experimentalists. Hopefully, experts on computational fluid dynamics find ways to improve.

2. Overview

The following gives an overview of the simulation method, leaving technicalities aside. The emphasis is on background, context, and the comparison with the experiment.

2.1. Linearization, Amplitudes of Oscillatory Motion

In FreqD-LBM, the populations are replaced by complex amplitudes, h_i . The index i labels the discrete velocities ($i = 0 \dots 8$ in 2D, $i = 0 \dots 18$ in 3D, when the D3Q19 stencil is employed, see Figure 2). For simplicity, the sets $\{h_i\}$ are called populations as in conventional LBM. Replacing the populations by complex amplitudes changes the interpretation but leaves the LBM algorithm largely unchanged. The most important difference is the term $-i\omega h$ in the collision operator. Also, nonlinear terms are omitted throughout. This is permissible because nonlinearities do not occur when the QCM is operated in a liquid (section 3.1).

2.2. Viscoelasticity, Limitations for Stiff Media

Because the entire formalism uses complex numbers, FreqD-LBM naturally covers viscoelasticity. In order to achieve that, the Newtonian viscosity, η , is replaced by $\tilde{\eta} = \eta' - i\eta''$. The dynamic

viscosity is related to the shear modulus as $\tilde{G} = i\omega\tilde{\eta}$. The kinematic viscosity, $\nu = \eta/\rho$, becomes complex, as well ($\tilde{\nu} = \nu' - i\nu''$) and the relaxation rate, τ^{-1} , becomes complex, in consequence (Equation 22). A “particle” is a domain with a large modulus of viscosity, $|\tilde{\eta}|$. The loss tangent, $\tan \delta = \eta''/\eta'$, can be chosen freely, in principle. However, convergence of the simulation can be slow when the system is elastic. Elasticity caused transient oscillations, which decay slowly.

A problem is encountered with rigid particles. If the viscosity is larger than the bulk viscosity by a factor of 100 or more, the simulation will not catch the difference between stiff particles and even stiffer particles. The difference between stiff and very stiff is unessential for particles freely suspended in the liquid and, also, for planar films with a thickness much less than the wavelength of sound. These act like rigid objects regardless of how stiff, exactly, they are. Whether or not the simulation catches the small deformation hardly makes a difference to the dynamics of the entire system. There is, however, such a difference for particles touching the resonator surface across a narrow contact. There is a stress concentration at the contact, which is not modeled well by the combination of streaming and collision. More generally, LBM deteriorates in accuracy when the relaxation time, τ , (Equation 20) is much larger than the time step in lattice units, which happens at large viscosity (section 5.4). The relaxation rate then is small. Improving the grid resolution ameliorates the problem (section 4.4) but improving grid resolution is computationally expensive, because the computation time scales as the 5th power of spatial resolution. It is difficult to employ a fine mesh only in certain critical regions (as is common in FEM).

2.3. Boundary Conditions

When a node is part of the boundary of the simulation box, the streaming step must account for the boundary condition. Three cases are to be distinguished:

- i. At the interface with the resonator surface, the streaming step is replaced by half-way bounce-back (Equation 12, ref. [30]). The bounce-back step reports the momentum transfer

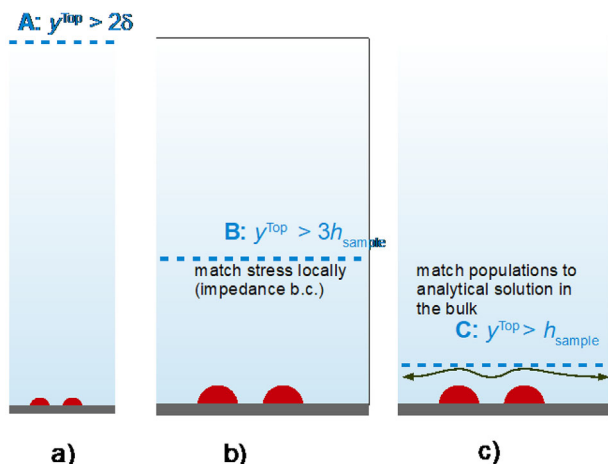


Figure 3. A) If the top of the simulation box is far outside the penetration depth of the shear wave, the boundary condition $u^T = 0$ is appropriate. B) If the boundary is inside the sheared layer, but at a height much larger than the height of the sample, a local non-reflective impedance boundary condition may be applied. C) For a boundary close to the sample, the populations are Fourier-decomposed. The different Fourier components are matched to the analytical solutions of the Stokes equation in the bulk.

to the resonator surface (Equation 13), which is equivalent to the xy-component of the stress to be inserted into Equation (2).

- ii. Periodic boundary conditions are applied in the plane of the sample (that is, along x and z). A problem occurs for the study of single particles because the periodic boundary conditions turn a single particle into a regular array of particles. When varying system parameters, interference maxima and minima are seen (Figure S18, Supporting Information to ref. [28]). These can be avoided by randomly placing a few particles (typically: three particles) in the simulation box and repeating the simulation with different such randomly generated configurations. Experience shows that the variability in the derived values of $\Delta f_n/n$ and $\Delta\Gamma_n/n$ is small (section 5.3, Figure 26).
- iii. The boundary condition at the interface to the bulk liquid cannot be given by zero velocity ($\vec{u}^T \equiv 0$, superscript T for “top”), because this would require the height of the cell to exceed the penetration depth of the shear wave, δ , by at least a factor of 2 (Figure 3A). δ obeys the relation $\delta = (2\nu/\omega)^{1/2}$. For 5 MHz resonators in water, δ is about 250 nm. The cell height would then have to be about 500 nm. Many samples of interest (proteins, vesicles), however, are only a few nanometers in diameter. Also, FreqD-LBM requires the grid resolution, Δx , to be much smaller than the penetration depth, δ . The simulation only solves the Stokes equation in this limit (section 4.1). If the cell height is comparable to δ , a considerable amount of computation time is spent on nodes far away from the adsorbate.

There are two solutions to this problem. First, one may formulate a local impedance boundary condition^[31] (Figure 3B). The velocity of the wall is chosen such that the boundary is locally non-reflective to shear waves. This set of equations is described in sections 9.1 and 9.3.

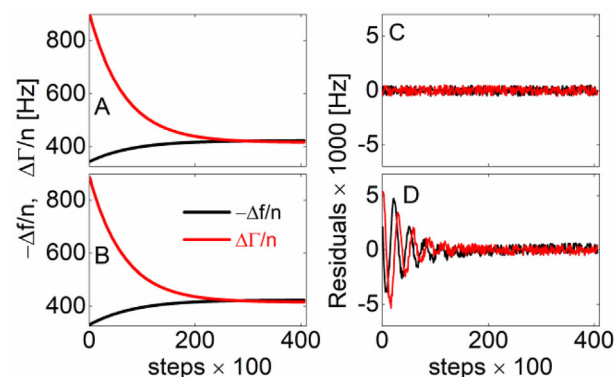


Figure 4. Two ring-in processes. Panels (A) and (B) show the simulation results and the fits with Equation 26 (indistinguishable). Panels C and D show the residuals. In panel D, the residuals contain oscillations. Their period is governed by a shear wave inside a sphere, experiencing multiple reflections at the sphere surface. The initial phase of the ring-in was discarded from these plots. Shortly after the oscillation of the substrate is started, the residuals are much larger than 0.01 Hz.

A more accurate method involves Fourier-decomposing the motion of the boundary and solving the equations of hydrodynamics in the bulk for the different in-plane wave-vectors (see sections 9.2 and 9.4). The amplitudes of these modes are then matched to the motion inside the simulation box (Figure 3C).

2.4. Ring-In

The target of the simulation is a periodic flow field with local amplitudes being stationary in time. The stationary state is found by starting from the quiescent state and turning on the oscillation of the substrate at time $t = 0$. A shear wave propagates into the liquid. The wave is distorted by the sample. It takes a few round-trip times of the wave to find the stationary state. The time for one round-trip is $2\tau_{RI} = 2n_y^2$. The subscript RI stands for ring-in. The extrapolation to infinite time is described in section 3.5.

The ring-in has nothing to do with the ring-down, that is used by some instruments to determine the resonance properties.^[32] Ring-down involves the resonator, whereas ring-in in FreqD-LBM does not.

2.5. Dynamics of Embedded Objects Treated Separately

FreqD-LBM loses accuracy when particles are too stiff (section 5.4). Stiff particles can still be modeled, if they are configured to be oscillating boundaries of the simulation box (Figure 5). The oscillation amplitudes at the points on the surface, where a link intersects the surface, must be chosen such that the forces exerted by the liquid match the forces of reaction, which are dictated by the properties of the embedded object. The force exerted onto the particle by the liquid follows from Equation (13). The force of reaction may involve the stiffness of the contact between the particle and the substrate. This stiffness can then be inferred from the comparison between simulation and experiment (section 7.2). As in the case of ring-in, the task is to find the stationary state. The amplitudes of motion of the particle need to be

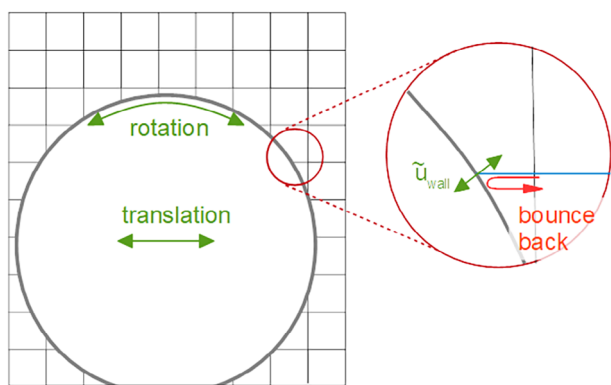


Figure 5. Objects, which are too stiff to be part of the simulation volume, must be modeled as oscillating boundaries. The oscillation amplitudes at the points on the surface, where the links intersect the surface, must be calculated such that the particle obeys the desired force balance. The force balance might take the stiffness of the contact into account. The calculation, which achieves that, is entirely analytical.

found by iteratively updating these amplitudes. Because the update must be slowed down artificially to avoid instabilities, the ring-in with embedded particles is slower than the ring-in without embedded objects. Also, the simulation no longer emulates the physical ring-in.

FreqD-LBM is flexible in how it calculates the force balance. The embedded objects might also be nanobubbles or liposomes. All that is needed is a way to calculate the amplitudes of oscillatory motion at the surface of these objects. These amplitudes are needed in the bounce back step. For nanobubbles, the calculation of the amplitudes involves the surface tension. For the liposomes, it involves the mechanics of the membrane.

2.6. Grid Resolution and Computational Efficiency

Among the drawbacks of FreqD-LBM is that the computation time per ring-in scales as the inverse 5th power of the grid resolution, Δx_{SI} . The first three powers follow from the number of nodes (typical: $20 \times 20 \times 20$ nodes). Two more powers follow from the ring-in time, τ_{RI} , being equal to n_y^2 . A typical ring-in requires a few 1000 steps. With $20 \times 20 \times 20$ nodes, a ring-in takes a few hours on an office PC, and a given simulation typically comprises many ring-ins involving different parameters, such as coverage and overtone order. Distributing the different ring-ins to different processor cores speeds up the simulation.

Distributing the relaxation step (which occurs locally on the nodes) to multiple GPUs would be another option. This step is technically more challenging than distributing the ring-in's to different CPUs. The possibility as such is one of the advantages of LBM. Note, however, that the relaxation step in FreqD-LBM is less demanding than in conventional LBM because the nonlinear terms are omitted. The relaxation step consists of Equation (18) and (19). The gain incurred by parallelizing the relaxation is not as large as in conventional LBM. Parallelization of the relaxation has not been carried out for FreqD-LBM yet.

2.7. Limitations in Accuracy

Sources of inaccuracies are:

- finite duration of the ring-in (section 2.4)
- insufficient grid resolution (section 2.6)
- insufficient height of the cell (section 5.2)
- insufficient lateral size of the box at low coverage
- insufficient statistics when randomly placing particles into the simulation box (section 7.1)
- problems with large viscosities (section 5.4)
- problems with finite compressibility (section 4.2).

The problems other than f) and g) can be mitigated by increasing the computational effort. Improving the grid resolution is particularly expensive. Simulations at low coverage are expensive because they require a large area. Compressibility is not a severe problem because the medium is almost incompressible, as it should be. Possibly, the compressibility can be made to match a certain target value with a collision operator using multiple relaxation times (sections 4.2 and 4.5, see also section 10 in ref. [22]).

At this point, one needs to keep in mind that there are substantial uncertainties in QCM experiments, as well. Often, one harmonic behaves unexpectedly with no obvious reason. The most likely cause are stronger-than-usual deviations of the vibration mode from pure thickness shear. Reproducibility between different QCM experiments typically is in the range of 10%. In ref. [34], the agreement between the simulation results and results obtained from a rigorous theory was in the range of 10%. Agreement between simulation and experiment is a challenge from both sides. In the authors' opinion, FreqD-LBM currently is the method of choice to address those numerous problems, where the answers leave room for uncertainties in the range of 10%.

2.8. Comparison with Adsorption Experiments

In QCM experiments on adsorption, the adsorption kinetics expressed as coverage versus time is only one out of a few targets. Problematic about coverage are the poorly understood effects of the trapped liquid.^[34] A quantification of the amount of trapped liquid based on FreqD-LBM is discussed in section 7 of the supporting information to ref. [28]. The mass per unit area as derived from $\Delta f_n/n$ with the Sauerbrey equation is sometimes called "wet mass". The wet mass differs from the dry mass by the mass of the trapped liquid. Note that the apparent wet mass usually depends on overtone order. A quantification of the wet mass is outside the scope here. The emphasis here is on non-gravimetric effects.

Given the trapped liquid, one should use $-\Delta f_n/n$ as a substitute for coverage and plot all other parameters versus $-\Delta f_n/n$. These plots look similar to plots versus coverage. Also, non-gravimetric effects are more easily discerned when the analysis is based on certain ratios of the shifts, rather than the shifts themselves. Along these lines, Tellechea et al. plotted $\Delta\Gamma/(-\Delta f)$ versus $-\Delta f_n/n$ and found characteristic features.^[35] $\Delta\Gamma_n/(-\Delta f_n)$ is called Df ratio. The plot is called "extrapolation scheme" in ref. [2]. Another ratio of interest is $1-(\Delta f_n/n)/(\Delta f_{n,\min}/n_{\min})$. "min" denotes the lowest overtone included in the measurement (often 15 MHz,

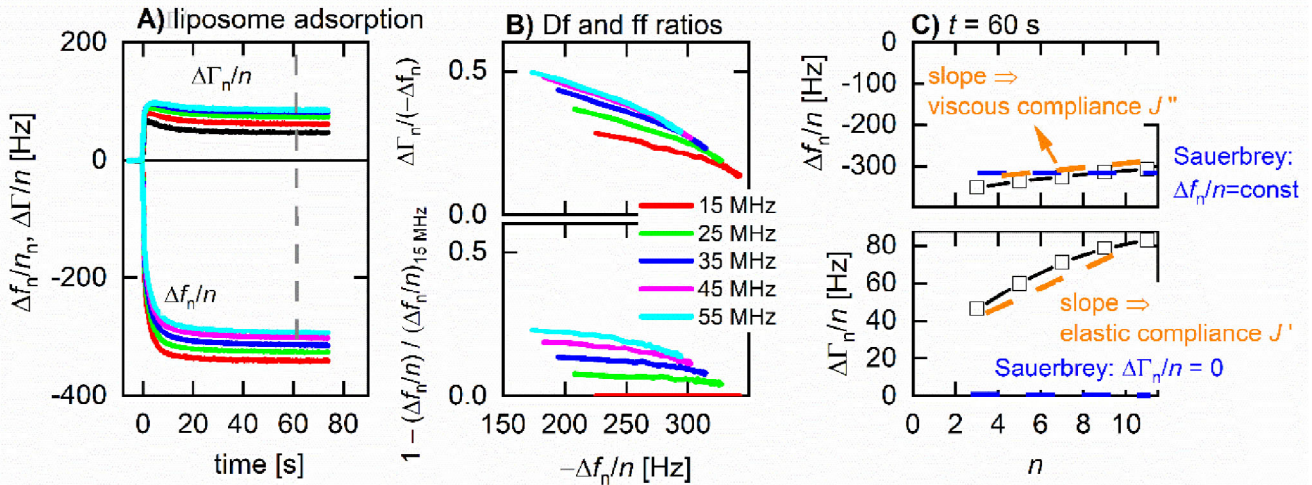


Figure 6. A) Adsorption of liposomes with radius of 35 nm to a QCM surface (data from ref. [36]). The experiment was configured such that the liposomes do not rupture (in which case they would have formed supported lipid bilayers). The values of $\Delta f_n/n$ shown in the lower part of panel (A) cannot directly be converted to coverage because of the unknown effects of the trapped liquid. Simulations undertaken for different coverages can therefore not be directly compared to the data from panel (A). B) The comparison becomes feasible, if ratios of the shifts are analyzed rather than the shifts themselves and if these are plotted versus $-\Delta f_n/n$. Diagrams of this kind can also be obtained from simulation. Both $\Delta \Gamma_n/(-\Delta f_n)$ (called “Df ratio”, top in panel B) and $1 - (\Delta f_n/n)/(\Delta f_n/n)_{15\text{MHz}}$ (called “ff ratio”, bottom in panel B) are zero in the Sauerbrey limit. These ratios quantify non-gravimetric effects. An example of simulation results plotted in this same way is shown in Figure 26. C) When $\Delta f_n/n$ and $\Delta \Gamma_n/n$ are plotted versus n , these plots look similar to what is obtained for planar viscoelastic films (section 4.6.2. in ref. [2]). Diagrams as shown in (C) can be interpreted in terms of the layer’s viscoelastic parameters. These would be “apparent” parameters for structured adsorbates because the adsorbates are not continuous media. Such apparent parameters would be input to an effective medium theory of the adsorbate. For a discussion of why the QCM results obtained on planar films look like what is shown in panel C, see section 4.6.2 in ref. [2]. Correction added on 17 March 2025, after first online publication: the reference number in figure caption 6A has been updated in this version.

might also be 5 MHz, but data from the fundamental often are discarded). The term $1 - (\Delta f_n/n)/(\Delta f_{n,\text{min}}/n_{\text{min}})$ is called ff ratio in the following. The ff-ratio defined this way is larger than zero because the values of $-\Delta f_n/n$ decrease with increasing overtone order for soft films. That fact that the apparent Sauerbrey mass as naively calculated from $-\Delta f_n/n$ decreases with increasing n , is called “missing mass effect” in ref. [37]. It is convenient to plot 1 minus the ratio rather than the ratio itself, because the former term is zero in the gravimetric limit, like the Df ratio. In the presence of non-gravimetric effects, the bandwidth is finite (leading to a non-trivial Df ratio) and $\Delta f_n/n$ differs between overtones (leading to a non-trivial ff ratio).

Figure 6A shows experimental data obtained while adsorbing liposomes with a radius of 35 nm. These liposomes did not rupture (did not form supported lipid bilayers). Figure 6B shows the Df ratios and ff ratios versus $-\Delta f_n/n$ as discussed above. Such data can be compared with data obtained with simulations such as the ones shown in Figure 26. The parameters underlying this latter simulation were not optimized to match Figure 6B. That can certainly be done, but there is the question of whether liposomes are well represented by the soft spherical particles treated in the simulation leading to Figure 26.

Figure 6C shows one single data set (the one at $t = 60$ s), where the shifts are plotted versus n . This plot is commonly used as the basis for fitting with a viscoelastic model. The difference between structured samples and planar samples does not become evident in plots of single sets of $-\Delta f_n/n$ and $\Delta \Gamma_n/n$ versus n . Plots of this kind showing data obtained from planar films look similar to Figure 6C. One might even use the plot shown in Figure 6C to

derive apparent values for the Sauerbrey thickness from the intercept of $\Delta f_n/n$ with the y-axis and an apparent viscoelastic compliance from the slopes (section 4.6.2 in ref. [2]). The interpretation of such apparent parameters pertaining to adsorbed liposomes is not obvious, though.

Distinguishing structured samples from planar samples is feasible based on plots of the Df ratio and the ff ratio versus $-\Delta f_n/n$ as shown in Figure 6B. When planar films grow in thickness, the Df ratio increases (assuming constant viscoelasticity). In contrast, the Df ratio decreases when particulate adsorbates increase in coverage (Figure 7). That the Df ratio decreases with increasing coverage can be rationalized by assuming that the layer becomes more compact and less compliant. Low compliance implies a small Df ratio. That the Df ratio increases for planar layers when their thickness increases requires a close look at the underlying equations (see, for instance, Equation 46 in ref. [2]). A similar set of arguments applies to the ff ratio.

3. Formulation of the Model

This section outlines the mathematics underlying FreqD-LBM. Comments on the code itself are provided in the documentation uploaded to GitHub.

In this section, we follow the terminology from ref. [22]. Also, we maintain variables in the equations, which have a fixed value. Examples are Δt and Δx (which both are equal to 1 in lattice units) and c_s^2 (the square of the speed of sound, equal to $1/3$ in lattice units). We do so because the equations then contain physical dimensions, which makes understanding easier. If SI

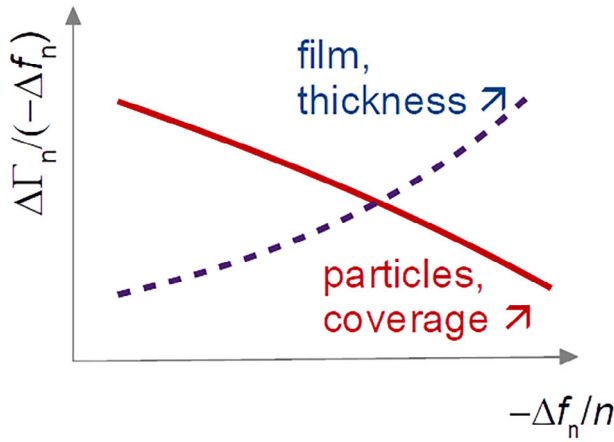


Figure 7. The dependence of the Df ratio on $-\Delta f_n/n$ characteristically differs between films of constant stiffness, which increase in thickness, and particulate adsorbates, which increase in coverage. The red curve corresponds to the top graph in Figure 6B.

are units are used, one can check for correct dimensions. Parameters in SI units are given the subscript SI. The populations $\{h_i\}$ have dimensions of density (kg/m^3 in SI units). The weight factors $\{w_i\}$ are dimensionless real numbers. The $\{c_i\}$ have dimensions of velocity (m/s in SI units). In some cases, the parameters with fixed values are replaced by the respective values in a second step. For example, $1/c_s^2$ then is replaced by 3. This is meant to show what the code looks like. The code uses the fixed values.

Section 3 assumes the density in lattice units to be constant ($\rho \equiv 1$). The extension to variable density is discussed in section 4.3. In this context, a reinterpretation of variables is proposed, which would alter the way equations are phrased in section 3. We stick to the formulation following ref. [22] here in order to facilitate the comparison to conventional LBM.

3.1. Linearized Models Apply

In the following, we discuss two sources of nonlinear stress-velocity relations, which are the advection term in the Navier-Stokes equation (given as $\rho(\mathbf{u} \cdot \nabla)\mathbf{u}$, components are $\rho \sum_i u_i \partial_i u_i$, quadratic in velocity, \mathbf{u}) and a nonlinear stress-strain relation of the materials involved. (A third such source would be the Lagrangian motion of particle surfaces.) The relative importance of the advection term is assessed with the Reynolds number, Re :

$$Re = \frac{\rho u L}{\eta} \quad (3)$$

L is a characteristic length. Choosing $L \approx \delta = (2\nu/(\omega))^{1/2}$ and estimating the velocity, u , as $u \approx \omega a$ with a the amplitude of oscillation, one arrives at

$$Re = \frac{\rho \omega a \delta}{\eta} = \frac{\omega a}{\nu} \sqrt{\frac{2\nu}{\omega}} = 2a \sqrt{\frac{\omega}{2\nu}} = 2 \frac{a}{\delta} \quad (4)$$

With $\delta \approx 100$ nm (depending on viscosity and overtone order) and $a < 1$ nm (true for resonators operated in liquids), one concludes that $Re \ll 1$.

There are different criteria for the onset of nonlinear stress-strain relations in rheology. In soft matter, one of the more stringent ones is that the strain energy per molecule should be less than $k_B T$.^[38] The energy density contained in the strain can be estimated as $G\gamma^2/2$ with $G = i\omega\eta$ the shear modulus and $\gamma \approx a/\delta$ the shear angle. Using $\eta \approx 1\text{mPa s}$, $\omega \approx 10^8 \text{ s}^{-1}$, $a \approx 1$ nm, and $\delta \approx 100$ nm leads to an energy density of $10 \text{ J}/\text{m}^3$. Assume a polymer with 1000 segments and a monomer weight of 100 atomic mass units. This leads to a volume per polymer chain of 166 nm^3 and a strain energy per molecule of less than $10^{-3} k_B T$.

Both estimates are confirmed in experiment. The shifts in frequency and bandwidth just about never depend on amplitude for experiments carried out in the liquid phase. This is different for point contacts in air.^[39,40] There are nonlinear effects in liquids, as well, but these are mostly caused by steady streaming.^[41–43]

3.2. Motivation of the Term $-i\omega h$ in the Collision Operator

FreqD-LBM simulates the approach of a quasi-oscillatory flow field to a stationary state, where the stationary state is purely oscillatory. The periodic flow field, $\bar{\mathbf{u}}(\mathbf{r}, t)$, and the oscillatory pressure field, $\bar{p}(\mathbf{r}, t)$, are written as

$$\begin{aligned} \bar{\mathbf{u}}(\mathbf{r}, t) &= \mathbf{u}(\mathbf{r}, t) \exp(i\omega t) \\ \bar{p}(\mathbf{r}, t) &= p(\mathbf{r}, t) \exp(i\omega t) \end{aligned} \quad (5)$$

Bold letters denote vectors. $\mathbf{u}(\mathbf{r}, t)$ and $p(\mathbf{r}, t)$ (without the bar) are complex envelopes, which eventually become stationary (and then only depend on \mathbf{r}). Because all amplitudes are small enough to let nonlinear effects be negligible, the Navier-Stokes equation turns into the Stokes equation:

$$\rho \frac{\partial \bar{\mathbf{u}}}{\partial t} = \nabla \left[\eta (\nabla \otimes \bar{\mathbf{u}} + (\nabla \otimes \bar{\mathbf{u}})^T) + \left(\eta_B - \frac{2}{3} \eta \right) \nabla \cdot \bar{\mathbf{u}} \right] - \nabla \bar{p} \quad (6)$$

Here, the superscript T denotes the matrix transpose. In the literature, the Stokes equation often contains an external volume force, which vanishes here. The term $\nabla \cdot \bar{\mathbf{u}}$ is negligible in liquids in the continuum limit. In FreqD-LBM, the medium is almost incompressible (section 4.2), which also justifies to neglect this term.

For the sake of the following simple motivation of the term $-i\omega h$, η is assumed to be constant. Constant η leads to

$$\frac{\partial \bar{\mathbf{u}}}{\partial t} = \frac{\eta}{\rho} \nabla^2 \bar{\mathbf{u}} - \frac{\nabla \bar{p}}{\rho} = \nu \nabla^2 \bar{\mathbf{u}} - \frac{\nabla \bar{p}}{\rho} \quad (7)$$

Inserting Equation (5) into Equation (7) leads to

$$\frac{\partial \mathbf{u}}{\partial t} \exp(i\omega t) + i\omega \mathbf{u} \exp(i\omega t) = \nu \nabla^2 \mathbf{u} \exp(i\omega t) - \frac{\nabla p}{\rho} \exp(i\omega t) \quad (8)$$

The term $\exp(i\omega t)$ cancels:

$$\frac{\partial \mathbf{u}}{\partial t} = \nu \nabla^2 \mathbf{u} - i\omega \mathbf{u} - \frac{\nabla p}{\rho} \quad (9)$$

Compared to Equation (6), Equation (9) contains the additional term $-i\omega\mathbf{u}$. This motivates the term $-i\omega h$ in the collision operator (Equation 19). For a proof that FreqD-LBM solves the equation $i\omega\bar{\mathbf{u}} = \nu\nabla^2\bar{\mathbf{u}}$ with constant ν in 1D see section 4.1. FreqD-LBM finds the decaying shear wave.

Viggen does not apply the term $-i\omega h$ in the collision step^[25] and does not find the same dispersion relations as we do in section 4.1.

3.3. Linearized Populations, Streaming, Bounce-Back

The dynamical variables are complex amplitudes of the oscillatory momentum densities. In the low-frequency limit, the complex amplitudes are almost real and the real part is related to the standard populations as^[23]

$$h_i = f_i - f_{\text{rest},i}^{\text{eq}} \quad (10)$$

$f_{\text{rest}}^{\text{eq}}$ are the populations in equilibrium at rest (equal to ρw_i). At finite frequency, the h_i become complex. For brevity, we call the h_i “populations”. Note that we do not normalize these amplitudes to $f_{\text{rest}}^{\text{eq}}$, as refs. [23] and [25] do. Without normalization, the equations from ref. [22] can be applied with few changes.

The amplitudes of the density modulation, $\Delta\rho$, and the amplitudes of velocities, u_α with $\alpha = x, y, z$, are related to the populations as

$$\begin{aligned} \Delta\rho &= \sum_i h_i & a) \\ u_\alpha &= \frac{1}{\rho} \sum_i h_i c_{\alpha,i} & b) \end{aligned} \quad (11)$$

As in standard LBM, the calculation proceeds as an alternation of streaming and collision steps. Again, the terms “collision” and “relaxation” are largely synonymous in this text. In the streaming step, all populations are replaced by the populations from the neighboring sites in the direction of $-c_i$. At the bottom and the top of the simulation box, the populations with velocities directed inwards are computed using half-way bounce-back.^[30] (Half-way bounce-back implies that the resonator surface is located at $y = -1/2$.)

Let the velocity of the wall be \mathbf{u}^W . Bounce-back prescribes the populations with velocities pointing into the simulation box as

$$h_i^{\text{in}}(t + \Delta t) = h_i^{\text{out}}(t) - 2\rho w_i \left(\sum_{\alpha=x,y,z} \frac{c_{i,\alpha} \cdot \mathbf{u}_\alpha^W}{c_S^2} \right) \quad (12)$$

The index i^- labels the velocity, which is opposite to the velocity with index i . The roles of i and i^- in Equation (12) are reversed compared to eq. 5.26 in ref. [22]. A list of correspondences between i^- and i is provided in the caption to Figure 2. The weight factors w_i are given in the caption to Figure 2, as well.

Bounce-back causes a force onto the wall, which for every velocity i is given as

$$F_{i,\alpha} = \frac{\Delta x^3}{\Delta t} (h_i^{\text{in}} + h_i^{\text{out}}) c_{i,\alpha} \quad (13)$$

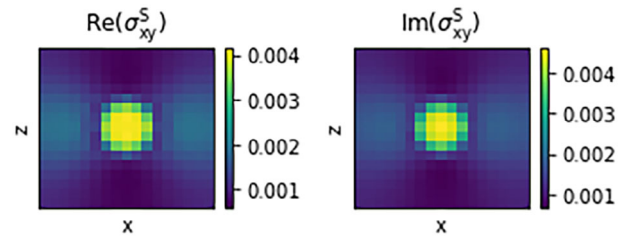


Figure 8. Plots of the real part and the imaginary part of the transverse stress at the resonator surface, $F_{x,S}$, produced by a sphere in the center of the box. The movement of the substrate occurs along the horizontal. Note that the single sphere really is a quadratic array of spheres because of the periodic boundary conditions. The stress between spheres is lowered compared to the stress exerted by the bulk liquid because the spheres couple to the surface not only across the contact, but also hydrodynamically across the liquid (Figure 9).

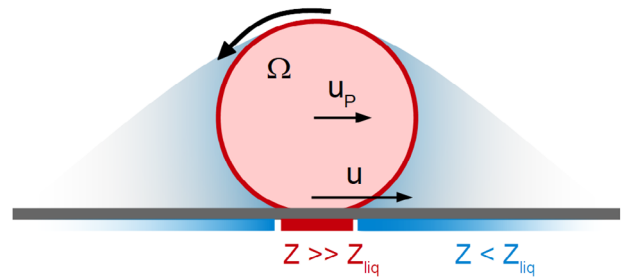


Figure 9. An illustration of how a sphere shields the adjacent portion of the surface from the shear stress exerted by the bulk liquid. In order to correctly determine the area-averaged stress, this type of screening must be accounted for. Adapted from ref. [28]

At the resonator surface, the velocity of the boundary is $\mathbf{u}^W = (1,0,0)$. Equation (12) turns into

$$h_i^{\text{in}}(t + \Delta t) = h_i^{\text{out}}(t) - 2\rho w_i \frac{c_{i,x} \cdot 1}{c_S^2} \quad (14)$$

Bounce-back at the bottom causes a momentum transfer to the surface (a force onto the surface), which for every velocity c_i is given as

$$F_{i,x} = \frac{\Delta x^3}{\Delta t} (h_i^{\text{in}} + h_i^{\text{out}}) c_{i,x} \quad (15)$$

The total transverse force at the respective site follows from summation over i . The area-averaged transverse stress, $\langle \bar{\sigma}^S \rangle_{\text{area}}$, which is needed in Equation (2), follows from averaging F_x over all nodes at the surface. The conversion from force to stress is trivial because the area per node is unity. **Figure 8** shows a typical stress distribution at the resonator surface obtained this way. Note that the spheres not only exert a stress at the contact, but that they also reduce the stress between the contacts. They shield this portion of the surface to some extent from the stress, which would otherwise be exerted by the bulk liquid (**Figure 9**).

When the particles are modeled as oscillating boundaries (section 2.5), interpolated bounce-back is applied, following ref. [44] and section 11.2.2.1 in ref. [22]. Let q be the ratio between the distance to the wall and the distance between the nodes. Two separate equations are needed, depending on whether q is smaller or

larger than 0.5. The equation to be applied for $q < 0.5$ is

$$h_i^{\text{in}}(t + \Delta t) = 2q h_i^{\text{out}}(t) + (1 - 2q) h_i^{+, \text{out}}(t) - 2\rho w_i \left(\sum_{\alpha=x,y,z} \frac{c_{i,\alpha} \cdot u_\alpha^W}{c_S^2} \right) \quad (16)$$

$h_i^{+, \text{out}}$ is the population at the node inside the liquid two steps away from the wall in the direction of $-c_i$. For the case of $q \geq 0.5$ the equation is

$$h_i^{\text{in}}(t + \Delta t) = \frac{1}{2q} h_i^{\text{out}}(t) + \left(1 - \frac{1}{2q}\right) h_i^{\text{in}}(t) - \frac{3}{q} 2\rho w_i \left(\sum_{\alpha=x,y,z} \frac{c_{i,\alpha} \cdot u_\alpha^W}{c_S^2} \right) \quad (17)$$

The momentum transfer (needed for the calculation of the movement of the embedded object) is again calculated with Equation (13).

3.4. The Collision Operator

In its most simple form, the collision step applies the Bhatnagar–Gross–Krook operator (the BGK operator, a relaxation with a single relaxation time).^[22,45] The populations are locally relaxed towards the equilibrium populations, h_i^{eq} . The equilibrium populations are calculated similarly to how they are calculated in standard LBM, but the nonlinear terms are omitted, which results in

$$h_i^{\text{eq}} = w_i \left(\Delta\rho + \rho \sum_{\alpha=x,y,z} \frac{c_{i,\alpha} \cdot u_\alpha}{c_S^2} \right) \quad (18)$$

$\Delta\rho$ and u_α are computed with Equation (11). If the BGK operator is employed, the relaxation step is

$$h^* = h + \frac{\Delta t}{\tau} (h^{\text{eq}} - h) - i\omega\Delta t h = h + \frac{1}{\tau} (h^{\text{eq}} - h) - i\omega h \quad (19)$$

The star denotes the post-collision state. The relaxation time τ is given as

$$\tau = \frac{\nu}{c_S^2} + \frac{\Delta t}{2} = 3\nu + \frac{1}{2} \quad (20)$$

ν is the kinematic viscosity. ν is 1/6 in lattice units for the bulk liquid, which leads to $\tau = \Delta t$ for the bulk liquid. In this case the collision step simplifies to

$$h^* = h^{\text{eq}} - i\omega h \quad (21)$$

When the kinematic viscosity is complex, τ^{-1} turns into a complex relaxation rate

$$\widetilde{\tau}^{-1} = \frac{1}{\frac{\nu}{c_S^2} + \frac{\Delta t}{2}} = \frac{1}{3(\nu' - i\nu'') + \frac{1}{2}} \quad (22)$$

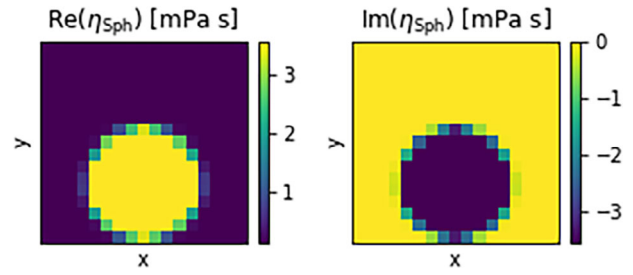


Figure 10. A plot of the viscosity in the simulation box with one particle in the center (a vertical cut through the center of the sphere).

Inside a particle, the bulk value of ν is multiplied by some complex factor. The modulus of this factor is equal to $|\eta_{\text{Sph}}|$ in units of mPa s, where the viscosity of the bulk liquid is assumed to be 1 mPa s. (The viscosity of water at room temperature is 0.89 mPa s.) The subscript “Sph” in the following denotes any object other than the bulk liquid (spherical or non-spherical).

A side remark on sign conventions. If the time dependence is written as $\exp(i\omega t)$, the complex kinematic viscosity must be written as $\nu' - i\nu''$. The minus sign ensures positive values of ν'' . If the time dependence is written as $\exp(-i\omega t)$, the sign before $i\nu''$ is positive. The complex frequency shift then is $\Delta f_n/n - i\Delta\Gamma_n/n$. In this text, the time dependence is written as $\exp(i\omega t)$.

Discretization errors are reduced by using interpolated viscosities for nodes, which are intersected by domain boundaries. More specifically, the viscosity is logarithmically interpolated:

$$\sqrt{\nu} = \exp\left(\phi_{\text{particle}} \log\left(\sqrt{\nu_{\text{particle}}}\right) + (1 - \phi_{\text{particle}}) \log\left(\sqrt{\nu_{\text{bulk}}}\right)\right) \quad (23)$$

Logarithmic interpolation is used because the reflectivity of a shear wave at a small step in viscosity follows the relation

$$r_{12} = \frac{Z_1 - Z_2}{Z_1 + Z_2} \approx \frac{\Delta Z}{2Z} \approx \frac{1}{2} \Delta(\ln Z) \quad (24)$$

The shear-wave impedance, Z , is proportional to $\nu^{1/2}$, hence the square roots in Equation (23). The contributions of the two adjacent domains to the volume of the respective node, ϕ_{particle} and $(1 - \phi_{\text{particle}})$, are determined by Monte-Carlo shooting. The algorithm randomly places a certain number of points into the cell and counts how many of them lie inside and outside the particle. **Figure 10** shows a vertical cut through the simulation box with color representing viscosity.

If needed, a local viscous stress can be computed as

$$\sigma_{\alpha\beta} = -\left(1 - \frac{\Delta t}{2\tau}\right) \sum_i c_{i,\alpha} c_{i,\beta} (h_i - h_i^{\text{eq}}) \quad (25)$$

For instance, the yy -component of the stress distribution close to the contact may be obtained using Equation (25) in order to calculate the torque at the contact.

Vertical cut, real parts, $n_z = 8$

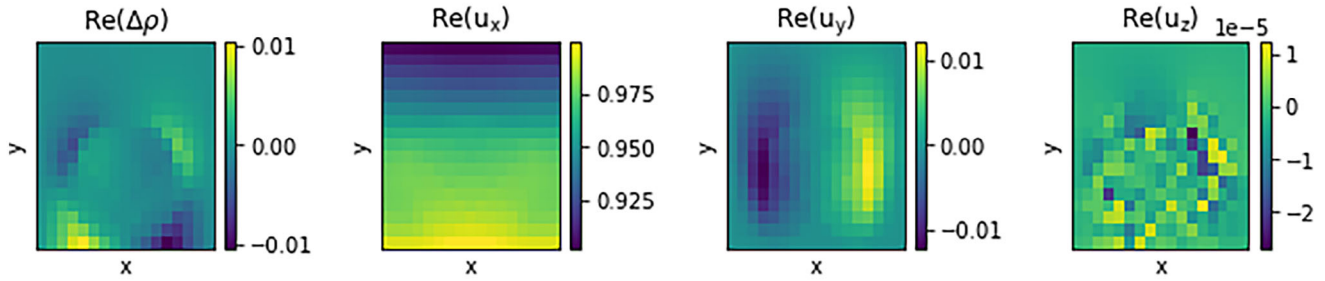


Figure 11. A vertical cut through a box containing one particle in the center. The cut intersects the center of the sphere. u_z is zero by symmetry.

3.5. Ring-In, Extrapolation to Infinite Time

The stationary state is found with what is called a “ring-in”. The oscillation of the resonator surface is started at time $t = 0$. A wave propagates into sample. After a certain time, the stationary state is reached, judged from the fact that $\Delta f_n/n$ and $\Delta \Gamma_n/n$, as calculated from the stress at the resonator surface, are almost constant.

Experience shows that $\Delta f_n/n$ and $\Delta \Gamma_n/n$ approach their final values in a pattern, which is robust and which can be used for extrapolation to infinite time. The time evolution of $\Delta f_n/n + i\Delta \Gamma_n/n$ can be fitted with the function

$$\frac{\Delta f_n + i\Delta \Gamma_n}{n} = \frac{\Delta f_{n,\text{extrap}} + i\Delta \Gamma_{n,\text{extrap}}}{n} + (A' + iA'') \exp(i(\omega_{\text{RI}}'t + i\omega_{\text{RI}}''t)) \quad (26)$$

t is the index of the iteration step. When $\Delta f_n/n$ and $\Delta \Gamma_n/n$ follow Equation (26) and when $\Delta \Gamma_n$ is plotted versus Δf_n in a polar diagram, a spiral is obtained. Only the center of the spiral is of importance. The parameters A' , A'' , ω_{RI}' , and ω_{RI}'' are not further analyzed. The parameters $(\Delta f_n/n)_{\text{extrap}}$ and $(\Delta \Gamma_n/n)_{\text{extrap}}$ are the basis for further interpretation. While Equation (26) can be motivated with the physics of the ring-in, we treat it as a heuristic fit function. (It is a good fit function if the initial part of the ring-in is discarded.) The question of when to terminate the calculation of the ring-in is part of the trade-off between accuracy and computation time. The extrapolation may become difficult, if there is a transient oscillation (Figure 4D).

3.6. Natural Scales and Conversion Between Lattice Units and SI Units

The following remarks apply to the fluid region. The most important scale of the problem is the penetration depth of the wave, δ (also called “Stokes length” or “viscous length”). The values of δ in lattice units and in SI units serve as a basis for the conversion between lengths in the two systems. δ is linked to the frequency by the relation

$$\delta = \left(\frac{2\nu}{\omega}\right)^{1/2} \quad (27)$$

from which it follows that

$$\omega = \frac{2\nu}{\delta^2} \quad (28)$$

In lattice units, the kinematic viscosity of the bulk is $1/6$. The values of ω in lattice units and in SI units provide for a conversion between the times in the two systems:

$$\Delta t_{\text{SI}} = \frac{\omega}{\omega_{\text{SI}}} \quad (29)$$

There is a second characteristic time linked to the ring-in, τ_{RI} , which is the time needed by the shear wave to reach the top of the simulation box. τ_{RI} is equal to n_y^2 with n_y the number of nodes along the vertical. It is equal to n_y^2 (rather than n_y) because the shear wave is diffusive in nature. The time needed to reach the stationary state is a few multiples of τ_{RI} .

Because $\omega \ll 1$, the time step is much smaller than the oscillation period. The entire ring-in is faster than the oscillation period because $\tau_{\text{RI}} = n_y^2 \ll \delta^2 = 2\nu/\omega = 4\nu/\pi \cdot T$ with T the oscillation period. This has far-reaching consequences for the underlying physics. Because the ring-in is fast, the oscillatory nature of the flow is less important than one might think. For quick estimates, one may replace the oscillatory shear wave by steady shear.^[10] Close to the surface, the two look rather similar. For instance, one might compare the transverse contact force exerted by a sphere, which is rigidly adsorbed to the resonator surface, with the result obtained by O’Neill in 1968,^[46] who calculated a similar force assuming steady shear. For the same reason, the real parts of most oscillatory amplitudes are larger than the imaginary parts close to the surface. When performing the various checks based on plots of certain amplitudes versus x , y or z , it usually suffices to display the real parts (cf. Figures 11 and 12). The term $\exp(i(\omega t - ky))$ is close to unity.

Because $\omega = 2\nu/\delta^2$, changing all lengths by some factor is equivalent to changing the frequency by the inverse square of the same factor. However, this scaling relation only holds if the viscosities are independent of frequency. The latter is not usually the case. In soft matter, there usually is viscoelastic dispersion, caused by stress relaxation on the time scale of the inverse oscillation frequency. Viscoelastic dispersion in the context of the QCM is discussed in section 4.7 of ref. [2]. In the context of the QCM, viscoelastic dispersion is most conveniently expressed in terms of power laws. If the absolute value of the shear modulus

Horizontal cut, real parts, $n_y = 17$

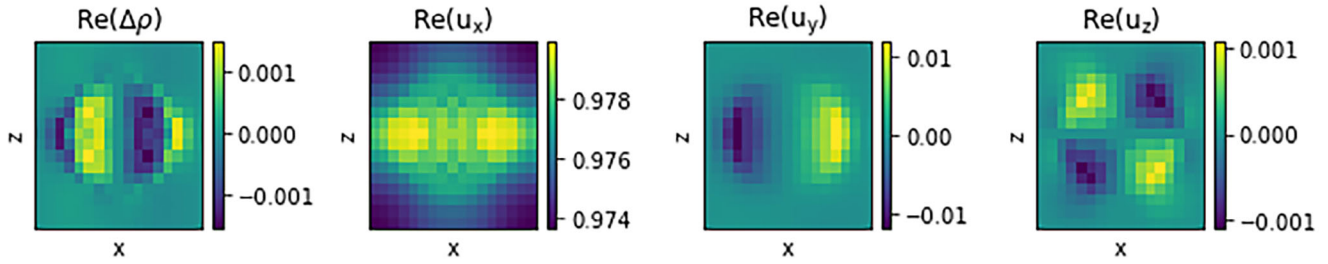


Figure 12. A horizontal cut through a box containing one particle in the center. The cut intersects the center of the sphere.

$|\tilde{G}|$ and the loss tangent $\tan \delta = G''/G'$ are used, the power laws spell out as

$$|G(f)| \approx |G_{\text{cen}}| \left(\frac{f}{f_{\text{cen}}} \right)^{\beta'} \quad (30)$$

$$\tan \delta(f) \approx (\tan \delta)_{\text{cen}} \left(\frac{f}{f_{\text{cen}}} \right)^{\beta''}$$

f_{cen} is a frequency in the center of the frequency range covered by the QCM (often $f_{\text{cen}} = 30$ MHz). $|G_{\text{cen}}|$ and $(\tan \delta)_{\text{cen}}$ are the values at this frequency. If the real and the imaginary part of the compliance, J' and J'' , are used, the power law is

$$J'(f) \approx J'_{\text{cen}} \left(\frac{f}{f_{\text{cen}}} \right)^{\beta'}$$

$$J''(f) \approx J''_{\text{cen}} \left(\frac{f}{f_{\text{cen}}} \right)^{\beta''} \quad (31)$$

The power law exponents, β' and β'' , differ between Equation (30) and (31). The use of J' and J'' rather than $|G|$ and $\tan \delta$ is advantageous for QCM problems because J' and J'' can be directly inferred from the slopes in plots as shown in Figure 6C (section 4.6.2 in ref. [2]). When interpreting differences between overtones, β' and β'' are part of this discussion.

The conversion between forces in the two systems is achieved with the mass of one volume element in lattice units and SI units. In SI units, it is $\Delta m_{\text{SI}} = \rho_{\text{SI}} \Delta x_{\text{SI}}^3$. The load impedance in SI units follows from the load impedance in lattice units as

$$Z_{L,\text{SI}} = Z_L \frac{\rho_{\text{SI}} \Delta x_{\text{SI}}}{\Delta t_{\text{SI}}^2} \quad (32)$$

3.7. Visualization of Velocity Fields

For the purpose of checking, the velocity fields and the field of oscillatory density can be displayed as contour plots. Figure 11 and Figure 12 shows such plots.

3.8. Calculation of Particle Velocities, Contact Forces, and Contact Torques

As always, the simulation gives access to properties of the sample, which are not accessible to experiment. Among these are the am-

plitude of oscillation of the sphere and the rate of rotation. These can be derived from the velocities inside the particle. The relative magnitudes of displacement and rotation are of importance for the discussion of the contact stiffness. If the displacement dominates, the sphere's dynamics is governed by the transverse contact stiffness. Otherwise, it is the bending stiffness.^[47] Similarly, the contact force and the contact torque can be derived from the local stress at the contact as obtained from Equation (25). The contact torque has no influence on $\Delta \tilde{f}/n$, following the small load approximation. Nevertheless, it is of much importance for the system's dynamics.

4. Validation

Below, it is proven that FreqDLBM reproduces steady plain shear waves and steady plain compressional waves in the limit of good grid resolution. The proof is limited to the stationary state, which is the case of relevance to the QCM. This is not meant to say that the ring-in was modeled unrealistically. On the contrary, the simulations suggest that the ring-in is reproduced correctly. In particular, one can assign a physical meaning to the transient oscillations, which sometimes are seen. Presumably, the oscillation seen in Figure 4D goes back to a wave inside a sphere, which experiences multiple reflections at the sphere surface. Only when the simulation box contains embedded objects, the motion of which is updated iteratively, does the simulation no longer reproduce the ring-in because the update must be slowed down artificially to avoid instabilities.

4.1. Shear Waves in 1D

The condition of stationarity can be used to prove that FreqDLBM solves the 2nd Stokes problem (the solution of which is the decaying shear wave). The calculation shown below requires $c_s \equiv 3^{-1/2}$ and $\rho \equiv 1$. For the case of $\rho \neq 1$ see section 4.3. The algebra is formulated using the D2Q9 stencil (left in Figure 2). From the condition that the populations after streaming and relaxation are the same as the initial populations, it will follow that $k^2 = -i\omega/\nu$, as required by the equation $i\omega u_x = \nu \nabla^2 u_x$.

Given that the displacement pattern is a shear wave, h_0, h_2 , and h_4 are zero. h_0 is the component associated with zero velocity. h_2 and h_4 are associated with velocities along the vertical. Further, $h_3 = -h_1, h_6 = -h_5$, and $h_7 = -h_8$. The problem has three dynamic

variables, which are h_1 , h_5 , and h_8 . In the streaming step, h_5 is replaced by the population from the line below, h_5^- , while h_8 is replaced by the population from the line above, h_8^+ . Population h_1 remains unchanged.

$$h_5 \rightarrow h_5^-, \quad h_8 \rightarrow h_8^+ \quad (33)$$

The shear wave is of the form $\exp(-iky)$ with k the wavenumber and y the surface normal. We seek to prove that FreqD-LBM

$$M \begin{pmatrix} h_1 \\ h_5 \\ h_8 \end{pmatrix} = \begin{pmatrix} 0 \\ 0 \\ 0 \end{pmatrix}$$

$$M = \begin{bmatrix} -i\omega - \frac{1}{3\tau} & & \frac{2+2ik-k^2}{3\tau} & & \\ \frac{1}{6\tau} & \frac{1}{6} \left(-6 + \left(1 + ik - \frac{k^2}{2} \right) \left(6 - 6i\omega - \frac{5}{\tau} \right) \right) & & \frac{2-2ik-k^2}{3\tau} & \\ \frac{1}{6\tau} & & \frac{1}{6} \left(1 + ik - \frac{k^2}{2} \right) & & \frac{2-2ik-k^2}{12\tau} \\ & & & \frac{1}{6} \left(-6 + \frac{1}{2} (-2 + 2ik + k^2) \left(-6 + 6i\omega + \frac{5}{\tau} \right) \right) & \end{bmatrix} \quad (40)$$

solves the 2nd Stokes problem in the limit of good grid resolution, which corresponds to small k in lattice units. The term $\exp(-ik\Delta y) = \exp(-ik)$ can therefore be Taylor-expanded to second order in k . Equation (33) turns into

$$h_5 \rightarrow h_5^- \approx h_5 \left(1 + ik - \frac{k^2}{2} \right), \quad h_8 \rightarrow h_8^+ \approx h_8 \left(1 - ik - \frac{k^2}{2} \right) \quad (34)$$

The velocity along x after streaming follows from

$$u_x = 2 \frac{1}{\rho} (h_1 + h_5^- + h_8^+) \quad (35)$$

The equilibrium populations to be used in the relaxation step are

$$h_1^{eq} = \frac{w_1}{c_s^2} \rho u_x = \frac{1}{3} u_x, \quad h_5^{eq} = \frac{w_5}{c_s^2} \rho u_x = \frac{1}{12} u_x,$$

$$h_8^{eq} = \frac{w_8}{c_s^2} \rho u_x = \frac{1}{12} u_x \quad (36)$$

The relaxation step (leading to populations with a star) is

$$h_1^* = h_1 + \frac{\Delta t}{\tau} (h_1^{eq} - h_1) - i\omega \Delta t h_1 = h_1 + \frac{1}{\tau} (h_1^{eq} - h_1) - i\omega h_1$$

$$h_5^* = h_5 + \frac{\Delta t}{\tau} (h_5^{eq} - h_5) - i\omega \Delta t h_5 = h_5 + \frac{1}{\tau} (h_5^{eq} - h_5) - i\omega h_5$$

$$h_8^* = h_8 + \frac{\Delta t}{\tau} (h_8^{eq} - h_8) - i\omega \Delta t h_8 = h_8 + \frac{1}{\tau} (h_8^{eq} - h_8) - i\omega h_8 \quad (37)$$

Stationarity requires that

$$h_1^* = h_1$$

$$h_5^* = h_5 \left(1 + ik\Delta y - \frac{(k\Delta y)^2}{2} \right) = h_5 \left(1 + ik - \frac{k^2}{2} \right) \quad (38)$$

$$h_8^* = h_8 \left(1 - ik\Delta y - \frac{(k\Delta y)^2}{2} \right) = h_8 \left(1 - ik - \frac{k^2}{2} \right)$$

and, in consequence

$$h_1 - \frac{1}{\tau} (h_1 - h_{eq,1}) - i\omega h_1 - h_1 = 0$$

$$h_5 - \frac{1}{\tau} (h_5 - h_{eq,5}) - i\omega h_5 - h_5 \left(1 + ik - \frac{k^2}{2} \right) = 0 \quad (39)$$

$$h_8 - \frac{1}{\tau} (h_8 - h_{eq,8}) - i\omega h_8 - h_8 \left(1 - ik - \frac{k^2}{2} \right) = 0$$

Inserting Equation (35) and Equation (36) into Equation (39) and expressing the result in matrix form leads to

The determinant of M must vanish. Taylor-expanding the determinant to second order in k and to first order in ω leads to

$$\det(M) \approx \omega \left(k^2 \left(-i + \frac{7i}{6\tau} \right) - \frac{i}{\tau^2} \right) + k^2 \left(\frac{1}{6\tau^2} - \frac{1}{3\tau} \right) = 0 \quad (41)$$

Using the BGK operator, the relaxation time τ is given as

$$\tau = \frac{\nu}{c_s^2} + \frac{\Delta t}{2} = 3\nu + \frac{1}{2} \quad (42)$$

Inserting Equation (42) into Equation (41) and solving for k^2 leads to

$$k^2 = -\frac{i\omega}{\nu} \quad (43)$$

This proves that FreqD-LBM indeed leads to decaying shear waves with the correct dispersion relation (the correct dependence of k on ω). Again, this result only holds in the limit of $k \ll 1$ in lattice units, which translates to $\Delta x \ll \delta$ (Figure 13).

Figure 13 demonstrates in more general terms that FreqD-LBM indeed solves the Stokes equation. Similar graphs are also provided in ref. [23]. On the right-hand side in Figure 13 the viscosity was made to be complex ($\nu = 1/6 \cdot (1-i)$). These simulations can be made to agree with the analytical result to any desired accuracy with sufficient grid resolution and sufficient ring-in time.

Whether Δx is small enough can be judged from the ratio $\Delta \Gamma_{\text{ref}} / (-\Delta f_{\text{ref}})$ in the absence of the sample. This calculation is always carried out prior to any ring-in in order to find the reference frequency. The reference frequency might also be calculated from the Gordon-Kanazawa relation.^[3] The cheap simulation of the reference state is done nevertheless, because some errors cancel when referencing the frequency shift obtained with the sample to the shift in the reference state as determined with a similar simulation. These errors include the apparent deviation in the

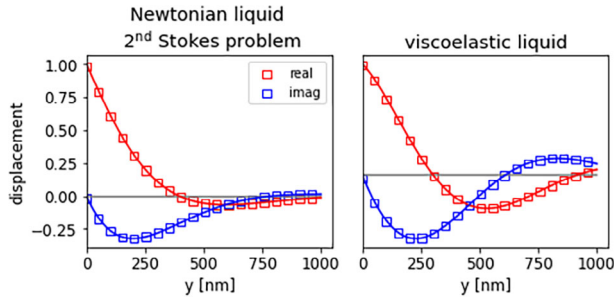


Figure 13. Displacement profiles in 1D obtained with a simulation of a Newtonian liquid ($\nu = 1/6$, left) and a liquid with a complex viscosity ($\nu = 1/6 \cdot (1 - i)$, right). y is the surface normal. The lines are the analytical results. A non-reflective impedance boundary as described in section 9.1 was applied at the top. The analytical solution is of the form $\exp(-iky)$ with $k = (\omega/(i\nu))^{1/2}$. The grid resolution was $\Delta x_{S1} = 10$ nm.

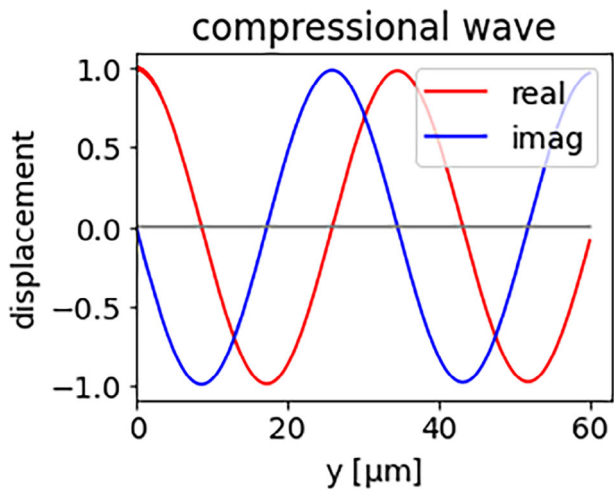


Figure 14. Displacement of a compressional wave at a frequency of 5 MHz. The grid resolution was $\Delta x_{S1} = 20$ nm. When the wave is displayed this way, the simulation result cannot be distinguished from the analytical result.

behavior of the Newtonian bulk liquid from Gordon-Kanazawa behavior (see below). The ratio $\Delta\Gamma_{ref}/(-\Delta f_{ref})$ should ideally be unity, following Gordon and Kanazawa, but in practice is slightly larger. The finite grid resolution introduces a fictitious viscoelasticity. For example, using $\Delta x_{S1} = 8$ nm, a frequency of 5 MHz, and a viscosity of $\eta = 1$ mPa s leads to $\Delta\Gamma_{ref}/(-\Delta f_{ref}) = 1.003$. A grid size of $\Delta x_{S1} = 8$ nm or less is not a problem when modeling adsorbed globular proteins because the grid resolution must be smaller than the feature size, anyway, and the height of the box will match that size. $\Delta x_{S1} = 8$ nm is a problem, when the objects under study exceed a size of about 50 nm. In particular, the lattice resolution must then be adapted to the overtone order because $\delta \propto n^{-1/2}$. Otherwise, the errors caused by the finite grid resolution depend on overtone order, which may create a fictitious dependence of $\Delta\tilde{f}_n/n$ on overtone order. Because the dependence of $\Delta\tilde{f}_n/n$ on overtone order is central to the analysis of non-gravimetric effects, care should be taken to not introduce such a dependence by letting $\Delta x/\delta$ strongly depend on n . A slight problem of this kind can be noticed in **Figure 17**. That argument is independent of whether the grid resolution suffices to catch

the geometry well enough. With regard to the latter question, we recommend Δx to be about 1/5 of the sphere radius, if spheres are to be modeled (section 5.1).

4.2. Compressional Waves in 1D

With compressional waves, the calculation proceeds similarly as in section 4.1. It is advantageous to use the D1Q3 stencil, which has three populations with velocities in the y -direction of 0, -1 , and $+1$. The weight factors are $\{2/3, 1/6, 1/6\}$. In the streaming step, h_2 is replaced by the population from the line below, h_2^- , while h_1 is replaced by the population from the line above, h_1^+ . Population h_0 remains unchanged.

$$h_1 \rightarrow h_1^-, \quad h_2 \rightarrow h_2^+ \quad (44)$$

The compressional wave is of the form $\exp(-iky)$ with k the wavenumber and y the surface normal. The populations after streaming are

$$h_1^- \approx h_1 \left(1 + ik - \frac{k^2}{2}\right), \quad h_2^+ \approx h_2 \left(1 - ik - \frac{k^2}{2}\right) \quad (45)$$

After the streaming step, the modulation in density, $\Delta\rho$, and the velocity along y , u_y , are

$$\Delta\rho = h_0 + h_1^- + h_2^+, \quad u_y = \frac{1}{\rho} (h_1^- - h_2^+) \quad (46)$$

The equilibrium populations to be used in the relaxation step are

$$h_0^{eq} = \frac{2}{3}\Delta\rho, \quad h_1^{eq} = \frac{1}{6}(\Delta\rho - 3\rho u_y), \quad h_2^{eq} = \frac{1}{6}(\Delta\rho + 3\rho u_y) \quad (47)$$

The relaxation step (leading to populations with a star) is

$$h_0^* = h_0 + \frac{1}{\tau} (h_0^{eq} - h_0) - i\omega h_0$$

$$h_1^* = h_1 + \frac{1}{\tau} (h_1^{eq} - h_1) - i\omega h_1 \quad (48)$$

$$h_2^* = h_2 + \frac{1}{\tau} (h_2^{eq} - h_2) - i\omega h_2$$

Stationarity requires that

$$h_0^* = h_0$$

$$h_1^* = h_1 \left(1 + ik - \frac{k^2}{2}\right) \quad (49)$$

$$h_2^* = h_2 \left(1 - ik - \frac{k^2}{2}\right)$$

and, in consequence

$$h_0 - \frac{1}{\tau} (h_0 - h_{eq,0}) - i\omega h_0 - h_0 = 0$$

$$h_1 - \frac{1}{\tau} (h_1 - h_{eq,1}) - i\omega h_1 - h_1 \left(1 + ik - \frac{k^2}{2}\right) = 0 \quad (50)$$

$$h_2 - \frac{1}{\tau} (h_2 - h_{eq,2}) - i\omega h_2 - h_2 \left(1 - ik - \frac{k^2}{2}\right) = 0$$

Inserting Equation (46) and Equation (47) into Equation (50) and expressing the result in matrix form leads to

$$M \begin{pmatrix} h_0 \\ h_1 \\ h_2 \end{pmatrix} = \begin{pmatrix} 0 \\ 0 \\ 0 \end{pmatrix}$$

$$M = \begin{bmatrix} -i\omega - \frac{1}{3\tau} & -\frac{1}{3\tau}(-2 - 2ik + k^2) & -\frac{1}{3\tau}(-2 + 2ik + k^2) \\ \frac{1}{6\tau} & -1 + \frac{1}{6}\left(1 + ik - \frac{k^2}{2}\right)\left(6 - 6i\omega - \frac{2}{\tau}\right) & \frac{1}{6\tau}(-2 + 2ik + k^2) \\ \frac{1}{6\tau} & \frac{1}{6\tau}(-2 - 2ik + k^2) & -1 + \frac{1}{6}(-2 + 2ik + k^2)\left(-3 + 3i\omega + \frac{1}{\tau}\right) \end{bmatrix} \quad (51)$$

Again, the determinant of M must vanish. Taylor-expanding the determinant to second order in k and to second order in ω , the determinant turns into

$$\det(M) \approx k^2\omega\left(-i + \frac{2i}{3\tau}\right) - \frac{k^2}{3\tau} + \omega^2\left(-k^2 + \frac{1}{\tau}\right) = 0 \quad (52)$$

Again, using the BGK operator (a single relaxation time, given as $\tau = 3\nu + 1/2$) and solving for k leads to

$$k_{comp} = k = \sqrt{3}\omega = \frac{\omega}{c_S} \quad (53)$$

$c_S = 3^{-1/2}$ was used in the second step. This is the expected relation.

Figure 14 graphically demonstrates that a compressional wave of the expected form is indeed obtained.

The speed of sound converted to SI units follows as

$$c_{S,SI} = \frac{1}{\sqrt{3}} \frac{\Delta x_{SI}}{\Delta t_{SI}} = \frac{1}{\sqrt{3}} \frac{\Delta x_{SI}}{\frac{\omega}{\delta^2}} = \frac{1}{\sqrt{3}} \frac{\Delta x_{SI}\omega_{SI}}{2\nu} \quad (54)$$

With a frequency of 5 MHz and $\Delta x_{SI} = 1$ nm, the speed of sound comes out to be 3500 m/s, to be compared with the literature value for water of 1500 m/s. The speed of sound can be made to agree with the literature value by suitably adjusting the grid resolution. However, a slightly incorrect compressibility is not expected to be a major cause of errors because the compressibility is small, anyway. The medium is almost incompressible. One will usually adjust the grid resolution for a desired balance between accuracy and computation time, accepting small errors linked to compressibility.

4.3. Spatially Variable Density

Variable density is of some practical importance because dry proteins usually have densities around 1.35 g cm^{-3} ,^[48] while the buffer has a density of about 1 g cm^{-3} .

Varying the density in FreqD-LBM involves a subtlety. Experience tells that spatially variable density can be accounted for by

- replacing the term $-i\omega h$ in the relaxation step with $-i\omega\rho h$ (ρ being the density in lattice units)
- *not* changing the kinematic viscosity accordingly ($\nu \equiv \eta$ in lattice units)
- *not* changing the parameter ρ in section 3 ($\rho \equiv 1$ in lattice units).

The film resonance (which allows for an easy comparison between simulation and the analytical result), is reproduced correctly with $\rho_{film} \neq 1$, using the term $-i\omega\rho_{film}h$ in the collision step (Figure 15). Simulating adsorbed spheres with increased density also leads to the expected increase in the apparent Sauerbrey mass Figure 16).

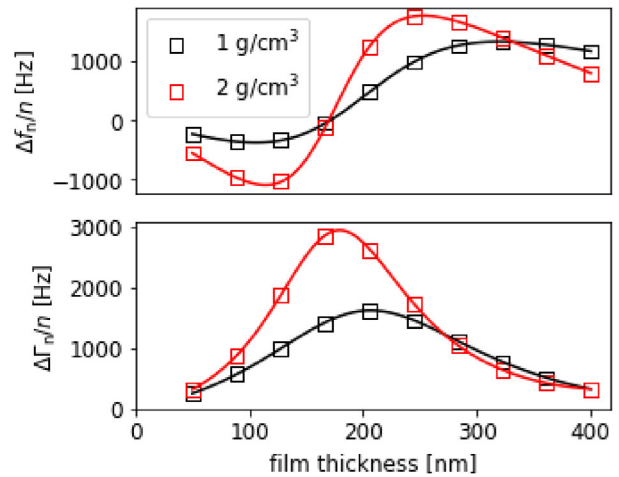


Figure 15. When the term $-i\omega h$ in the collision operator is replaced by $-\rho/\rho_0 i\omega h$, the film resonance is reproduced correctly. The density pertains to the film. The lines were calculated with Eq 69.

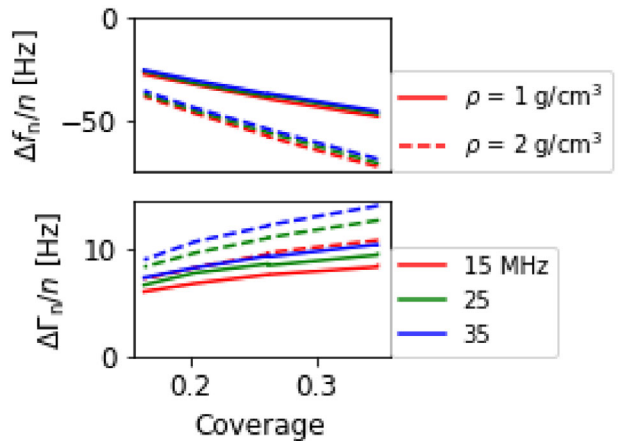


Figure 16. When the term $-i\omega h$ in the collision operator is replaced by $-\rho/\rho_0 i\omega h$, the frequency shift induced by adsorbed spheres of increased density lets $\Delta f_n/n$ decrease. $\Delta f_n/n$ is not strictly proportional to the density of the spheres because of the liquid between the spheres.

The physical meaning of this approach can be clarified by reinterpreting the variables. The reinterpretation must occur under the constraint that the parameter c_s stays equal to $3^{-1/2}$ in lattice units. The discretization in velocity ($f(\mathbf{x}, |\mathbf{v}|, t)$ being replaced by the $f_i(\mathbf{x}, t)$) requires certain relations between the $\{c_i\}$ and c_s . If c_s^2 is made to differ from $1/3$, the simulation produces unphysical results.

The steps in reinterpretation are the following:

- i. The density is viewed as the product of the number density, ρ_N , and a mass per particle, m . The number density is assumed as unity everywhere. The mass per particle, m , can be spatially variable.
- ii. h , u , and w are all viewed as momentum densities. The term ρ then disappears from all equations in section 3.3. $\Delta\rho$ in Equation 11a is replaced by the fractional change in density, $\Delta\rho/(\rho_N m)$. Unit times and unit lengths must be included in some instances to let the physical dimensions be correct.
- iii. All terms of the form $\sum_\alpha (c_{i,\alpha} u_\alpha)/c_s^2$ are replaced by $\sum_\alpha (c_{i,\alpha} u_\alpha \Delta x^3)/(k_B T)$. Such terms occur in Equation (12) and Equation (18). c_s^2 in the denominator is replaced by $k_B T$ (which still is $1/3$ in lattice units). This is the key difference. c_s^2 is equal to RT (Eqs 1.21 and 12.2d in ref. [22] with R being equal to k_B/m). Since there now is a term m in the numerator, R can be equal to k_B (making peace with the Avogadro constant being unity).
- iv. The relaxation time in the collision step is viewed as a ratio of a viscosity and some elastic modulus. This is the orthodox view in soft-matter physics. The elastic modulus usually is the high-frequency shear modulus (often called G_∞). Here, it is the modulus of compression of the ideal gas, which is equal to the pressure. Following the ideal gas law, $p = k_B T \rho_N$. Given that $\rho_N \equiv 1$ in lattice units, one may write

$$\tau = \frac{\eta}{k_B T \rho_N} + \frac{\Delta t}{2} = 3\eta + \frac{1}{2} \quad (55)$$

The relaxation time defined this way is independent of the mass per particle, m .

- i. The replacement $-i\omega h \rightarrow -i\omega\rho h$ amounts to a conjecture. Rather than motivating the term with the product rule (as was done section 3.2), it is interpreted as a small change in momentum density, resulting from streaming and relaxation. It occurs with a negative sign in the streaming step, because the populations are amplitudes of oscillatory motion.

The replacement $-i\omega h \rightarrow -i\omega\rho h$ in the calculation of the dispersion relation for shear waves (section 4.1) at first glance leads to $k^2 = -i\omega\rho/v$, which is incorrect. However, the correct result is obtained, if τ from Equation (42) is replaced by τ from Equation (55).

The replacement $-i\omega h \rightarrow -i\omega\rho h$ in the calculation of the dispersion relation for compressional waves (section 4.2) leads to $k = \omega\rho/c_s$. That is strictly incorrect, even if c_s is made to scale as $\rho^{-1/2}$. That does not make a large difference in quantitative terms, because the (small) compressibility is slightly incorrect, anyway.

The following equations collect the changes applied to the equations from sections 3.3 and 3.4. $\{h_i\}$, $\{u_\alpha\}$, and $\{w_i\}$ are momentum densities (SI units: $\text{kg m}^{-2} \text{s}^{-1}$). $\{c_i\}$ are velocities. In lat-

tice units, one has $\rho_0 \equiv 1$, $\rho_N \equiv 1$, $\Delta t \equiv 1$, $\Delta x \equiv 1$, and $k_B T \equiv 1/3$.

$$\begin{aligned} \frac{\Delta\rho}{\rho_N m} &= \frac{1}{\rho_N m} \frac{\Delta t}{\Delta x} \sum_i h_i \quad a) \\ u_\alpha &= \sum_i h_i \left(c_{i,\alpha} \frac{\Delta t}{\Delta x} \right) \quad b) \end{aligned} \quad (56)$$

$$h_i^{\text{in}}(t + \Delta t) = h_i^{\text{out}}(t) - 2w_i \left(\sum_{\alpha=x,y,z} \frac{c_{i,\alpha} \cdot u_\alpha^W \Delta x^3}{k_B T} \right) \quad (57)$$

$$F_{i,\alpha} = \frac{\Delta x^3}{\Delta t} \left(h_i^{\text{in}} + h_i^{\text{out}} \right) \left(c_{i,\alpha} \frac{\Delta t}{\Delta x} \right) \quad (58)$$

$$h_i^{\text{in}}(t + \Delta t) = h_i^{\text{out}}(t) - 2w_i \frac{c_{i,x} \cdot 1 \Delta x^3}{k_B T} \quad (59)$$

$$F_{i,x} = \frac{\Delta x^3}{\Delta t} \left(h_i^{\text{in}} + h_i^{\text{out}} \right) \left(c_{i,x} \frac{\Delta t}{\Delta x} \right) \quad (60)$$

$$\begin{aligned} h_i^{\text{in}}(t + \Delta t) &= 2q h_i^{\text{out}}(t) + (1 - 2q) h_i^{+, \text{out}}(t) \\ &\quad - 2w_i \left(\sum_{\alpha=x,y,z} \frac{c_{i,\alpha} \cdot u_\alpha^W \Delta x^3}{k_B T} \right) \end{aligned} \quad (61)$$

$$\begin{aligned} h_i^{\text{in}}(t + \Delta t) &= \frac{1}{2q} h_i^{\text{out}}(t) + \left(1 - \frac{1}{2q} \right) h_i^{\text{in}}(t) \\ &\quad - \frac{3}{q} 2w_i \left(\sum_{\alpha=x,y,z} \frac{c_{i,\alpha} \cdot u_\alpha^W \Delta x^3}{k_B T} \right) \end{aligned} \quad (62)$$

$$h_i^{\text{eq}} = w_i \left(\frac{\Delta\rho}{\rho_N m} + \sum_{\alpha=x,y,z} \frac{c_{i,\alpha} \cdot u_\alpha^W \Delta x^3}{k_B T} \right) \quad (63)$$

$$h^* = h + \frac{\Delta t}{\tau} (h^{\text{eq}} - h) - i \frac{\rho}{\rho_0} \omega \Delta t h = h + \frac{1}{\tau} (h^{\text{eq}} - h) - i\omega\rho h \quad (64)$$

$$\tau = \frac{\eta}{k_B T \rho_N} + \frac{\Delta t}{2} = 3\eta + \frac{1}{2} \quad (65)$$

$$h^* = h^{\text{eq}} - i\omega\rho h \quad (66)$$

$$\widetilde{\tau}^{-1} = \frac{1}{\frac{\eta}{k_B T \rho_N} + \frac{\Delta t}{2}} = \frac{1}{3(\eta' - i\eta'') + \frac{1}{2}} \quad (67)$$

$$\sigma_{\alpha\beta} = - \left(1 - \frac{\Delta t}{2\tau} \right) \sum_i \left(c_{i,\alpha} \frac{\Delta t}{\Delta x} \right) \left(c_{i,\beta} \frac{\Delta t}{\Delta x} \right) \frac{\Delta x}{\Delta t} (h_i - h_i^{\text{eq}}) \quad (68)$$

4.4. Planar Layers: the Film Resonance

The propagation of plane waves in stratified Δx media is governed by two parameters, which are the speed of propagation and the wave impedance, Z . The latter governs the reflectivity at interfaces. The amplitude of reflection at a step in impedance is given as $r_{12} = (Z_1 - Z_2)/(Z_1 + Z_2)$.

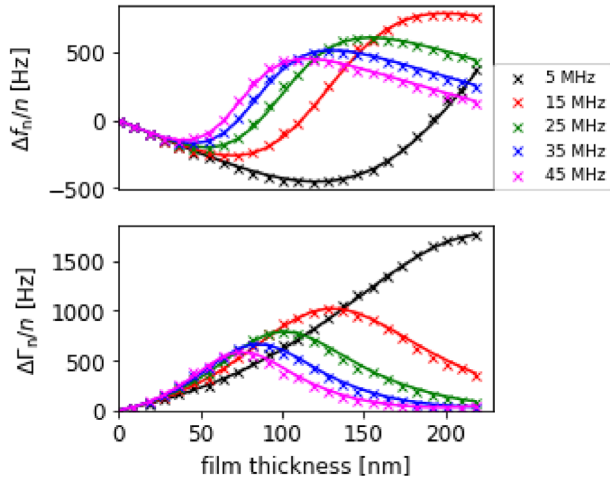


Figure 17. The simulation reproduces the film resonance. The viscosity was $|\eta_{\text{Film}}| = 1.67 \text{ mPa s}$, $\tan \delta = 0.2$. The grid resolution was $\Delta x_{\text{SI}} = 5 \text{ nm}$.

Extending calculations of the kind shown in section 4.1 to this problem leads to complicated algebra. The medium would have to contain a step in viscosity. Given the complications, this check was only done numerically, reproducing the film resonance with a simulation. The film resonance occurs, because shear waves are reflected at the interface between a film and the bulk liquid. An interference pattern is seen when the film thickness is about $\lambda/4$ with λ the wavelength of shear sound. For more details on the film resonance see section 4.5.4 in ref. [2].

Figure 17 shows $\Delta f_n/n$ and $\Delta \Gamma_n/n$ versus film thickness, d_f , as produced by a viscoelastic film. The analytical result (shown as lines in Figure 17) is^[49]

$$\frac{\Delta f + i\Delta \Gamma}{n} = \frac{if_0}{n\pi Z_q} \cdot \left[i\tilde{z}_f \frac{\tilde{z}_f \tan(\tilde{k}_f d_f) - i\tilde{z}_{\text{liq}}}{\tilde{z}_f + i\tilde{z}_{\text{liq}} \tan(\tilde{k}_f d_f)} - i\tilde{z}_{\text{liq}} \right] \quad (69)$$

On high overtones, the film resonance occurs at lower film thicknesses, because the wavelengths of shear sound are shorter. Close inspection shows that there are slight deviations between the simulation and the analytical result on the high overtones. They are more pronounced on the high overtones because the ratio $\Delta x/\delta$ increases with increasing n (remember that $\delta \propto n^{-1/2}$), effectively decreasing the grid resolution.

The agreement between simulation and the analytical result is less impressive, when the viscosity of the film is around 50 mPa s. This problem is discussed in section 5.4.

4.5. Oscillating Cylinder in a Viscous Fluid

The next three test cases go beyond shear waves. They also involve interpolated bounce-back from surfaces, which make an angle with the axes of the grid. In principle, the oscillating sphere in a viscous liquid would be a natural test case. The ratio of force to velocity (the friction coefficient, ξ_{fric}) for this configuration is well known.^[50] Because of the periodic boundary conditions, the simulation needs large system size (≥ 100 nodes in all three dimensions). It turned out that the size of the simulation box was prohibitively large for the simulations in 3D. In 2D, the simula-

tion is feasible. The results discussed below were obtained with the D2Q9 stencil. Similar plots are also shown in ref. [23].

The oscillating cylinder in a viscous medium was discussed as early as 1851 by Stokes.^[51] Note that the oscillating cylinder does not lead to a divergence in force at infinite box size (as the steadily moving cylinder does, the latter being the “Stokes paradox”).

We base the comparison with analytical theory on Equation (5) in ref. [53], which is

$$\xi_{\text{fric}} = -2\pi (K' - iK)$$

$$K = \left(\frac{R_{\text{Cyl}}}{\delta} \right)^2 + 2 \frac{R_{\text{Cyl}}}{\delta} + \frac{R_{\text{Cyl}}/\delta}{8 (R_{\text{Cyl}}/\delta + 0.34)^2} \quad (70)$$

$$K' = 2 \frac{R_{\text{Cyl}}}{\delta} + 1 - \frac{R_{\text{Cyl}}/\delta}{8 (R_{\text{Cyl}}/\delta + 0.107)^2}$$

ξ_{fric} is the ratio of the force per unit length to the velocity. R_{Cyl} is the radius of the cylinder. Note that there is no resonator involved in this simulation. The flow is driven by the cylinder in the center of the cell, which oscillates perpendicular to its axis.

Ref. [53] simplifies a more general equation for a certain range of parameters. The more general equation is^[23]

$$\frac{\xi_{\text{fric}}}{\rho R^2 \omega} = -\pi i \left(1 - \frac{4K_1(\sqrt{i\beta})}{K_1(\sqrt{i\beta}) + \sqrt{i\beta} K_1' \sqrt{i\beta}} \right) \quad (71)$$

$$\beta = \frac{\omega R^2}{\nu} = 2 \frac{R^2}{\delta^2}$$

K_1 is one of the modified Bessel functions of the second kind.

The lines on the left-hand side in **Figure 18** were calculated with Equation (70). The agreement with the simulation can be improved with enlarged cell size and better grid resolution (not shown). As **Figure 18** shows, the results improved slightly, when the MRT operator from section 10.4.1 in ref. [22] was employed. The choice of parameters proposed there leads to vanishing compressibility. Whether this result implies that multiple relaxation times will always improve accuracy, is open at this point. Also, the MRT operator in 3D is rather complicated.

4.6. Shallow Surface Roughness

As a further validation step, we compare the results from FreqD-LBM with an analytical result for the frequency shift induced by a corrugated surface.^[53–55] For a single sinusoidal wave, Urbakh and Daikhin predict:

$$\frac{\Delta f_n}{n} = -\frac{f_0}{n\pi Z_q} \sqrt{\frac{\omega \rho \eta}{2}} \left[\frac{h_{\text{UD}}^2}{l_{\text{UD}}^2} \left(2\cos^2 \phi - \frac{l_{\text{UD}}}{\delta} \right) \right]$$

$$\frac{\Delta \Gamma_n}{n} = \frac{f_0}{n\pi Z_q} \sqrt{\frac{\omega \rho \eta}{2}} \left[\frac{h_{\text{UD}}^2}{l_{\text{UD}}^2} \left(\frac{l_{\text{UD}}}{\delta} \right) \right] \quad (72)$$

h_{UD} is the amplitude of the sinusoidal corrugation (“corrugation” in **Figure 19**). l_{UD} is its wavelength (set to 20 nm in **Figure 19**, equal to the width of the cell). (In other papers on roughness by

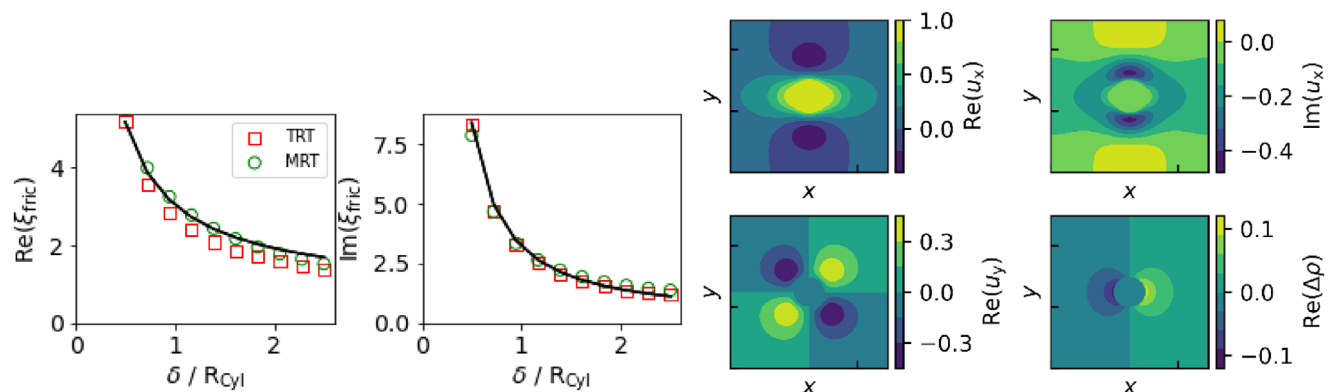


Figure 18. Calculation of the force-velocity ratio (the friction coefficient, ξ_{fric}) for an oscillating cylinder in a 2D Newtonian liquid. The cylinder radius was 10 nm. The frequency was varied, which lets δ vary accordingly. The grid resolution was $\Delta x_{\text{SI}} = 1$ nm. The solid line is the result from Equation (70). The graphs on the right show snapshots. "TRT" on the left denotes relaxation with two relaxation times following Equation 75 with $\Lambda_{\text{TRT}} = 1/4$. „MRT" denotes relaxation with multiple relaxation times, following section 10.4.1 in ref. [22]. The moments were arranged to let η_B in Equation 10.27 from ref. [22] be infinite. The MRT operator gave slightly better results than the TRT operator.

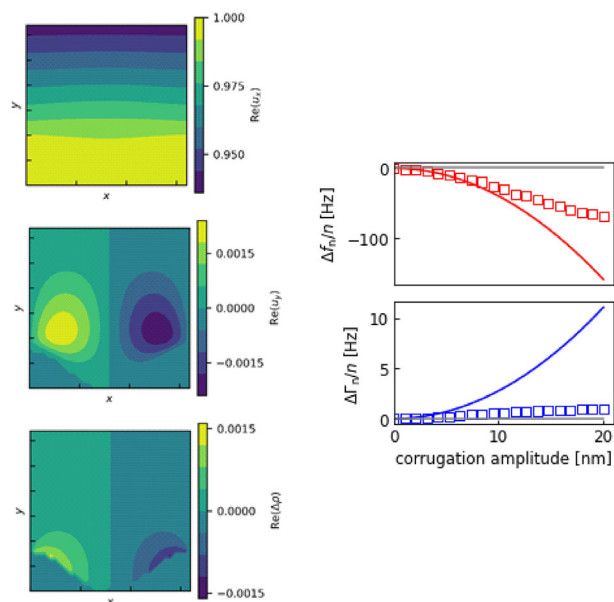


Figure 19. Left: Real parts of the velocity amplitudes along x (in the plane) and y (normal to the surface) as well as the changes in density above a corrugated surface. The width and the height of the cell were 20 nm, both. The corrugation was ± 2 nm. The grid resolution was $\Delta x_{\text{SI}} = 0.6$ nm. Grey lines denote the zero. The graph on the right compares the shifts in frequency and bandwidth as obtained with the simulation (open squares) with the prediction from Equation (72) (solid lines). There is agreement in the limit of shallow corrugation ($h_{\text{UD}}/l_{\text{UD}} < 5\%$).

the Tel-Aviv group, l is the lateral characteristic length of a random rough surface. It is the wavelength of a sine wave here.) ϕ is the angle between the k -vector of the corrugation wave and the direction of oscillatory movement (the x -direction). The prefactor corresponds to the Gordon-Kanazawa result^[3,4] (flat surface in a Newtonian liquid).

Figure 19 shows the results of these simulation. The simulation reproduces the Urbakh-Daikhin prediction in the shallow-corrugation limit. The Urbakh-Daikhin result is only valid in this

limit. The agreement is within the uncertainty inherent to the simulation as long as the amplitude of corrugation is less than 5% of the wavelength.

4.7. Spheres Floating Freely Above the Surface

As the last validation step, we simulate a free-floating sphere above the resonator surface, for which an analytical result has been found by the Leshansky group.^[56] The cell contains a single sphere at some distance from the surface. The full lines in Figure 20 show the predictions derived in ref. [57]. The calculation assumes a large distance of the sphere from the surface. The simulation and the analytical formula agree to within about 10 %. That concerns the shifts of frequency and bandwidth, the transverse velocity of the sphere, u_x , and the angular velocity, Ω_z .

A side remark concerns particles, which are rigidly attached to the resonator surface (rather than free-floating). These have also been modeled by the Leshansky group.^[33] Good agreement with the FreqD-LBM results and – also – with experimental results from the Krakow group^[10] was found.

5. Limitations

5.1. Grid Resolution

The most severe limitation of FreqD-LBM presumably is grid resolution. Typically, the number of nodes is $20 \times 20 \times 20$. Figure 21 shows simulation results obtained with a single sphere located in the center of the box. The truncation at the bottom was 5%. The viscosity of the sphere was $|\eta_{\text{Sph}}| = 100$ mPa s. The loss tangent was 3. Clearly, the results were found to depend on grid resolution. From this figure, it was concluded that choosing $\Delta x_{\text{SI}} = R_{\text{Sph}}/5$ is a reasonable compromise between accuracy and computational effort. At this choice, the number of steps was about 2500, the number of nodes was about 70 000, and the computation time per ring-in was about 4 hours on a workstation 2x Intel Xeon CPU X5675 @3.07 GHz (24 GB RAM). To obtain an ini-

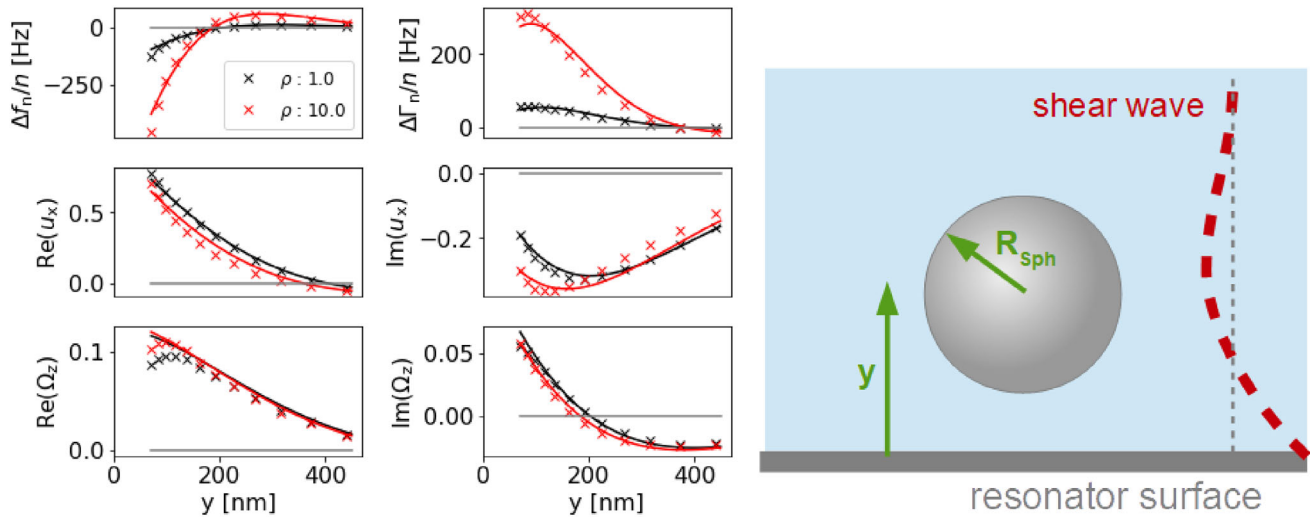


Figure 20. Comparison between simulation results (symbols) and the analytical prediction from ref. [56] (lines). The sphere radius was $R_{\text{sph}} = 63$ nm. The frequency was 5 MHz. u_x and Ω_z are the amplitudes of displacement along x and of rotation about the z -axis.

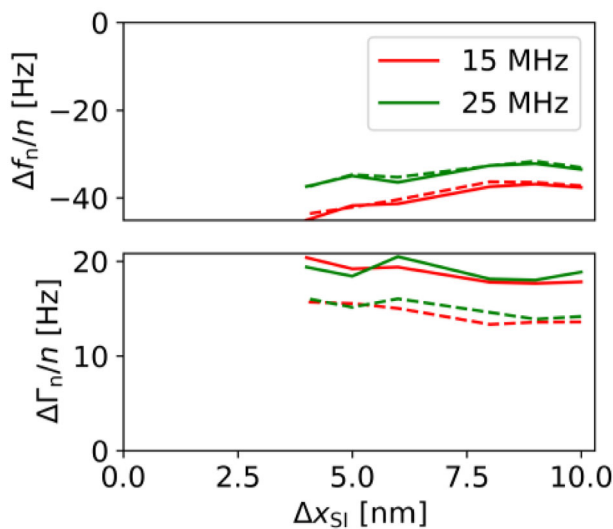


Figure 21. Frequency and bandwidth shifts as a function of grid resolution. The parameters were $R_{\text{sph}} = 30$ nm, $|\eta_{\text{sph}}| = 100$ mPa s, $\tan \delta = 1$ (solid lines) or $\tan \delta = 3$ (dashed lines). It is concluded that a reasonable compromise between accuracy and computation time is $\Delta x_{\text{SI}} = R_{\text{sph}}/5$ (corresponding to $\Delta x_{\text{SI}} = 6$ nm in the graph).

tial overview, $\Delta x_{\text{SI}} = R_{\text{sph}}/2.5$ also works. The latter choice speeds up the computation (compared to $\Delta x_{\text{SI}} = R_{\text{sph}}/5$) by a factor of $2^5 = 32$.

5.2. Distance of the Upper Boundary from the Top of the Sample

Placing the upper boundary of the cell as low as possible speeds up the ring-in. By default, FreqDLBM uses the more advanced version of the boundary condition, which is based on a Fourier decomposition of the flow field (section 9.4). If spheres are to be simulated, the values of the shifts as a function of the width of the gap between the sample and the upper boundary level off

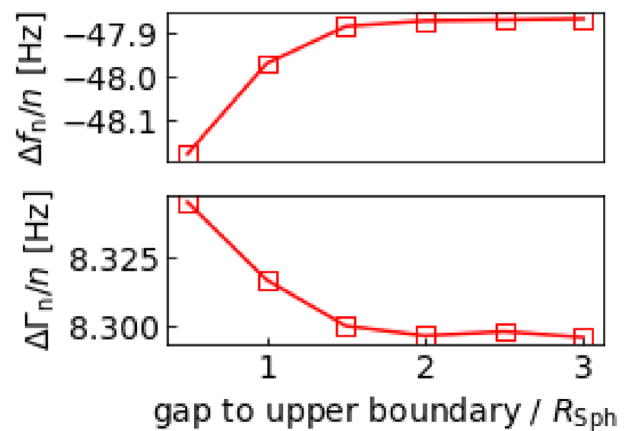


Figure 22. If the upper boundary of the simulation box is too close to the sample, $\Delta f_n/n$ and $\Delta \Gamma_n/n$ depend on the width of the gap between the sphere and the boundary. This dependence levels off at a gap width of $1.5 \cdot R_{\text{sph}}$. This width is the default value.

at a gap width of $1.5 \cdot R_{\text{sph}}$ (Figure 22). This is the default value. The gap between the sample and the top should be wider than 1.5 times the characteristic feature size of the sample. This limit occurs, because the calculations from section 9.4 require small amplitudes of normal motion.

5.3. Influence of Clustering

The fact that randomly placing three spheres in the simulation box leads to values of $\Delta f_n/n$ and $\Delta \Gamma_n/n$ with low scatter between different runs comes as a slight surprise. That was most thoroughly tested for soft spheres. For stiff spheres, the scatter tended to be larger. This leads to the question of how sensitive the QCM is to whether particles adsorb as clusters or more randomly. That issue shall be addressed in future work.

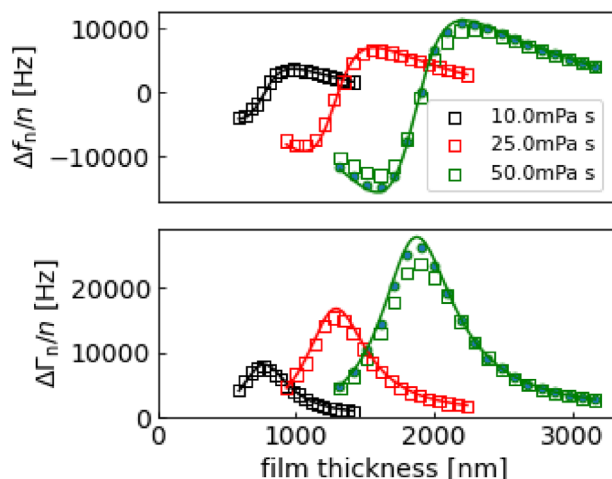


Figure 23. A simulation of the film resonance illustrating the problems at high viscosity. The loss tangent was $\tan \delta = 0.2$ in all cases. The grid resolution was 25 nm for the data shown as squares. At large viscosity, the deviations between the simulation and the analytical result increase. The green dots show data obtained with improved grid resolution ($\Delta x_{S1} = 12.5$ nm instead of 25 nm). Improving grid resolution ameliorates the problems seen at high viscosity. The thickness at which the resonance occurs increases with viscosity because the wavelength increases.

5.4. Large Viscosity

When the viscosity becomes large, the relaxation rate in the collision step becomes small and the populations rush through the respective domains without sufficient equilibration. Section 3.5.3.1 in ref. [22] calls this problem “under-relaxation”. LBM works best, when the relaxation time is around unity.

Figure 23 illustrates the problem using the film resonance as an example. At $|\eta_{\text{film}}| = 50$ mPa s the problem becomes noticeable (\times in green). The problem can be ameliorated by halving Δx_{S1}

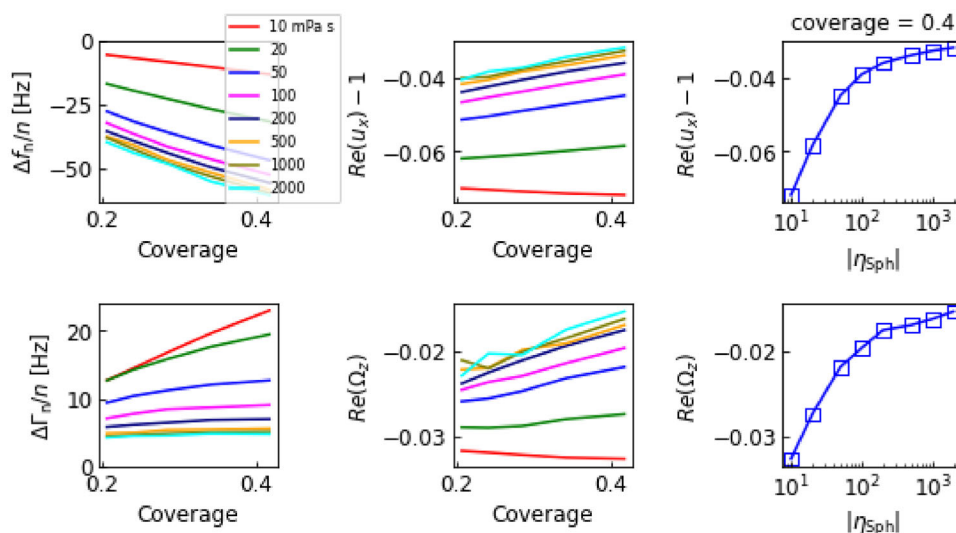


Figure 24. Results from a simulation conducted similarly to the ones described around Figure 26. Only the overtone at 15 MHz was simulated. The loss tangent was $\tan \delta = 1$. The data in the center and on the right show the amplitudes of the tangential displacement of the sphere center, u_x , and rotation, Ω_z . At viscosities of larger than 100 mPa s, the amplitudes of motion level off, rather than decreasing further, as they should.

(dots in green) because the populations then have more time to equilibrate with the domain.

As a second illustration of the problem, **Figure 24** shows simulation results obtained on “soft” adsorbed particles, similar to the ones shown in **Figure 26**. Differing from **Figure 26**, the viscosity spans a wide range. The spheres with a viscosity of 2000 mPa s should act like rigid particles. They should no longer move. Such spheres might still increase the bandwidth because they disturb the liquid flow. Nonzero $\Delta \Gamma$ alone is not evidence of a movement of the spheres. The plot of the Df ratio in the center of **Figure 24** is also not conclusive in this regard. The plots on the right-hand side show the sphere’s amplitudes of movement. The very stiff sphere ($|\eta_{\text{sph}}| = 2000$ mPa s) still moves appreciably. The amplitude is not much reduced compared to the sphere with a viscosity of 100 mPa s. At viscosities higher than 100 mPa s, the high viscosity is no longer recognized as such. Such spheres must be modelled as embedded objects with the oscillating boundary method (section 2.5).

6. Open Questions

The authors are experimentalists. They have encountered problems, which require the attention of experts on the lattice Boltzmann method. These are briefly summarized in the following.

6.1. A More Intuitive Treatment of Density

In section 4.3 it was reported that variable density can be accounted for (as far as we can tell) by replacing the term $-i\omega h$ in the collision step by the term $-i\rho/\rho_0\omega h$. This amounts to a conjecture. Justification or—better—a more consistent treatment of the entire formalism would be desired.

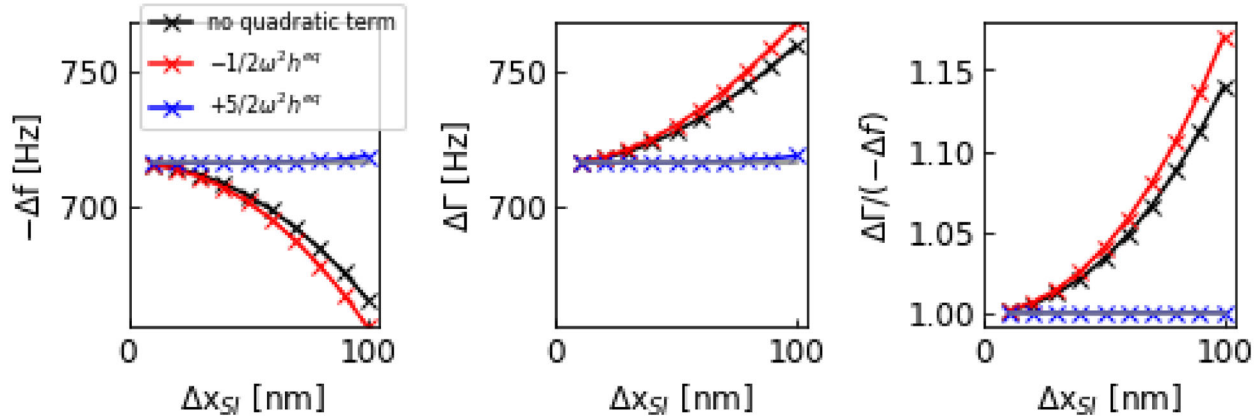


Figure 25. Shifts of frequency and bandwidth as simulated for the semi-infinite Newtonian liquid. The parameters of the simulation were $f = 5$ MHz, $\eta = 1$ mPa s, and cell height = 1000 nm. A non-reflective local boundary condition following section 9.1 was applied at the top. Gordon and Kanazawa predict $-\Delta f = \Delta\Gamma = 716$ Hz (grey horizontal line).^[3] This result is also obtained by the simulation in the limit of small Δx_{S1} . When Δx_{S1} is increased, deviations are seen, which are not removed by the quadratic term following ref. [23]. The agreement does become better, though, if quadratic term is chosen to be $+5/2 \omega^2 h^{eq}$ rather than $-1/2 \omega^2 h^{eq}$.

6.2. Second-Order Accuracy

Shi and Sader in ref. [23] add the term $-i\omega h - \omega^2/2h^{eq}$ in the collision step, rather than the term $-i\omega h$. This term follows from a Chapman-Enskog analysis. The ω^2 -term is supposed to ensure “second-order accuracy”. The calculation makes sense and including the term in the collision step comes at no additional cost in terms of computation time. “Second-order accuracy” would be very attractive because it would allow the grid resolution to be reduced. Increased Δx_{S1} implies increased ω in lattice units (Equation 28) and an increased time step in SI units (Equation 29).

However, that is not confirmed in the simulation. The test can be done based on the complex frequency shifts induced by a semi-infinite Newtonian liquid. The analytical result as derived by Gordon and Kanazawa is $-\Delta f = \Delta\Gamma = 716$ Hz for $f = 5$ MHz and $\eta = 1$ mPa s. Figure 25 shows these simulations. Including the quadratic term following ref. [23] (data in red) does not improve the agreement. It actually makes it slightly worse.

There is an interesting side aspect this test. If the term $-\omega^2/2 h^{eq}$ is replaced by $+5/2 \omega^2 h^{eq}$ and if, further, the relaxation time in lattice units is unity, the agreement does become better. Possibly, the difference goes back to the fact that ref. [23] normalizes the populations the populations at rest, while we do not. This finding has far-reaching consequences for the treatment of particles modeled as oscillating boundaries. In these simulations, the bulk liquid has $\tau = 1$. The quadratic term can be applied and the grid resolution can be lowered. $\Delta x_{S1} = 30$ nm (at 5 MHz) is acceptable. The quadratic term also improves accuracy for $\tau \neq 1$, but the improvement is less impressive than in Figure 25.

We attempted to justify this finding by including the term $+5/2 \omega^2 h^{eq}$ into the analysis from section 4.1. However, that only succeeds if the quadratic term is $-5/2 \omega^2 h^{eq}$. When the quadratic term is included, Equation (34) is replaced by

$$\begin{aligned} h_5 &\rightarrow h_5^- \approx h_5 \left(1 + ik - \frac{k^2}{2} - \frac{ik^3}{6} + \frac{k^4}{24} \right), \\ h_8 &\rightarrow h_8^+ \approx h_8 \left(1 - ik - \frac{k^2}{2} - \frac{ik^3}{6} + \frac{k^4}{24} \right) \end{aligned} \quad (73)$$

Equation (37) is replaced by

$$\begin{aligned} h_1^* &= h_1 + \frac{1}{\tau} (h_1^{eq} - h_1) - i\omega h_1 - \frac{5}{2} \omega^2 h_1^{eq} \\ h_5^* &= h_5 + \frac{1}{\tau} (h_5^{eq} - h_5) - i\omega h_5 - \frac{5}{2} \omega^2 h_1^{eq} \\ h_8^* &= h_8 + \frac{1}{\tau} (h_8^{eq} - h_8) - i\omega h_8 - \frac{5}{2} \omega^2 h_1^{eq} \end{aligned} \quad (74)$$

The Taylor expansion of the determinant (see the sentence before Equation 41) is carried out to 4th order in k and to second order in ω . The final result (Equation 43) then contains a 2nd-order term in ω , which vanishes when $\tau = 1$ and when the quadratic term is $-5/2 \omega^2 h^{eq}$. Note again the negative sign. The simulation underlying Figure 25, on the other hand, succeeds if the quadratic term is $+5/2 \omega^2 h^{eq}$. A renewed, consistent treatment in the frame of Chapman-Enskog theory is needed.

The quadratic term does not vanish, if analogous replacements are made in section 4.2, treating the compressional wave. As long as the compressibility is small, the difference is unessential.

6.3. Calculation of the Populations in the Stationary State from the Condition of Stationarity

In principle, the calculation of the populations might also be based on the condition of stationarity, similar to the calculations in sections 4.1 and 4.2. The condition that all populations are the same before and after a streaming-collision cycle fixes the populations. A large, sparse, inhomogeneous system of linear equations is obtained, where the source term is the motion of the resonator surface. Solving this equation system rather than simulating the ring-in would (presumably) make the program run faster.

6.4. Two and More Relaxation Times

Ref. [22] recommends the use of the two-relaxation-time operator (the TRT operator) rather than the BGK operator. Two relaxation

times come at no additional cost in terms of computation time. FreqDLBM offers the TRT operator. The TRT operator contains a “magic” parameter Λ , which can be chosen for optimum performance with respect to specific tasks (section 10.7.2 in ref. [22]).

When applying the TRT operator, the populations are split in two halves, where the second half contains the populations with directions opposite to those of the first half (indices i). New populations are defined as the sums and the differences of these pairs. The sums and differences are relaxed with different relaxation times and the original populations are recovered. The equations are:

$$\begin{aligned} \tau_{Symm}^{-1} &= \tau^{-1}, & \tau_{Asym}^{-1} &= \frac{4 - 2\tau^{-1}}{2 - \tau^{-1} + 4\Lambda_{TRT}\tau^{-1}} \\ h_{Symm,i} &= \frac{1}{2} (h_{i(i)} + h_i) & h_{Asym,i} &= \frac{1}{2} (h_{i(i)} - h_i) \\ h_{Symm,i}^{eq} &= \frac{1}{2} (h_{i(i)}^{eq} + h_i^{eq}) & h_{Asym,i}^{eq} &= \frac{1}{2} (h_{i(i)}^{eq} - h_i^{eq}) \\ h_{Symm,i}^* &= h_{Symm,i} - \tau_{Symm}^{-1} (h_{Symm,i}^{eq} - h_{Symm,i}) - i\omega h_{Symm,i} \\ h_{Asym,i}^* &= h_{Asym,i} - \tau_{Asym}^{-1} (h_{Asym,i}^{eq} - h_{Asym,i}) - i\omega h_{Asym,i} \\ h_i^* &= h_{Symm,i}^* - h_{Asym,i}^* \\ h_{i(i)}^* &= h_{Symm,i}^* + h_{Asym,i}^* \end{aligned} \quad (75)$$

Experience shows, that the TRT operator with $\Lambda_{TRT} = 1/4$ gives better results than BGK operator for the film resonance, when the viscosity is high.

For the reasons discussed in section 10.7.3 of ref. [22], using even more relaxation times may allow to actively control the compressibility. Section 10.4 in ref. [22] only discusses examples in 2D. The values proposed there did improve the agreement between the simulation and the analytical result in section 4.5 (oscillating cylinder in a viscous medium, 2D geometry, Figure 18). Whether or not a collision step with multiple relaxation times can improve the compressibility in 3D is open at this point.

6.5. Code Optimization and Parallelization

The code uploaded to Github was written in Python. The Numba package is used to accelerate some critical parts. Different rings can be distributed to different CPUs. Up to now, the code does not distribute the collision step to many GPUs. That would further improve performance.

6.6. Solution of the Equations of Hydrodynamics and Viscoelasticity in 3D with the Finite Element Method (FEM)

This work is not meant to say that FreqD-LBM was more powerful than the other methods of computational fluid dynamics. FEM and the finite volume method, FVM, in particular, allow to adapt mesh to the geometry. The authors understand that there are special problems with solving the incompressible Navier-Stokes equation with FEM in 3D.^[57,58] Possibly, experts can solve these.

6.7. Vary System Parameters in a Wide Range and Use the Results for Machine Learning

There is a vast array of possible configurations. Doing numerous such simulations, certain patterns are noticed. For instance, the degree of truncation often does not matter much, which can be rationalized by effects of increasing contact stiffness compensating the effects of decreased sample height. In this case, a rule is found, which can be understood. One might search for similar rules more systematically. One might sample the configuration space, feed the simulation results into a machine learning algorithm, and thereby arrive at rules, which give the experimentalist first clues for interpretation without the need to actually do the simulations. That would be part of an automation effort.^[59–62]

7. Applications

This section discusses three application examples. The first two are concerned with adsorption of soft and stiff spheres. Experiments of this kind motivated the development of FreqD-LBM. The third example is more special. It is meant to demonstrate how flexible the technique is.

7.1. Adsorption of Soft Particles

Figure 26 shows simulation results on the adsorption of soft particles. Basically, the data look similar to what is shown in Figure 6. Similar results (less accurate) were also reported in ref. [28]. The error bars are standard deviations from three runs with different randomly positioned particles (three particles). The error bars are hardly discernible for the shifts themselves (see also section 5.3). Panel (B) shows the Df ratios and ff ratios. The Df ratios are in line with extrapolation scheme. The Df ratios can be extrapolated to the point of intersection with the x-axis. The value of $\Delta f_n/n$ at the point of intersection leads to the height of the sample when converted to d_{Sau} with Equation (1). For more details see ref. [28].

The dependence of the Df ratio and the ff ratio on $-\Delta f_n/n$ and n can be fitted with straight lines. Four free parameters (offsets and slopes) capture the result well.

7.2. Adsorbed Rigid Particles, Contact Stiffness

Figure 27 shows an attempt to quantitatively interpret the experimental data obtained by the Krakow group on the adsorption of silica spheres to the resonator surface.^[10] This description is brief. For more details see ref. [29]. Spheres are modeled as embedded objects (section 2.5). The spheres are only allowed to undergo a translation along x with amplitude u_x and to rotate about the z -axis with amplitude Ω_z . The rotation occurs about the point of contact.

The spheres stay almost undeformed apart from a small region close to the contact. More specifically, the viscoelastic parameters are the same everywhere inside the sphere, but the deformation only is appreciable close the contact because of the large stress at the contact. This situation has been analyzed analytically

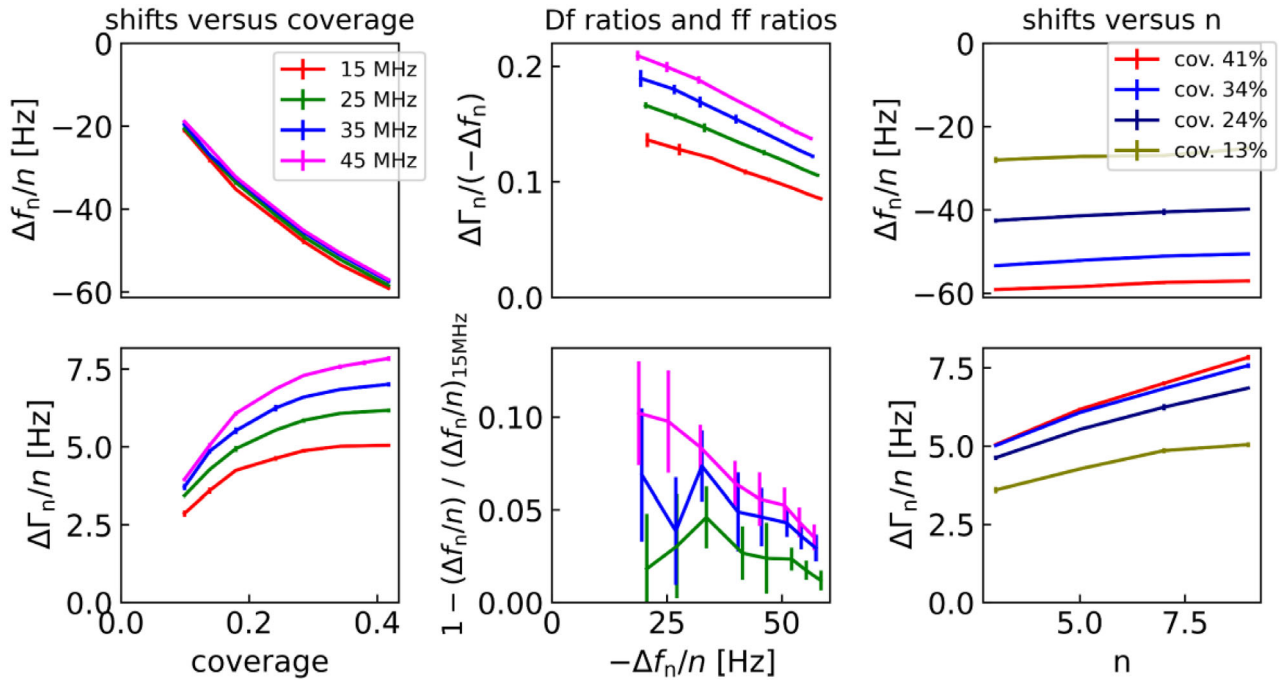


Figure 26. A simulation reproducing experiments where spheres are adsorbed to the resonator surface. Only data from panels in the center can be compared with the experiment because these do not contain coverage. The coverage is not accessible to the experimentalist. The slopes in the center panels evidence the particulate nature of the sample (cf. Figure 6 and Figure 7). The data in the panel on the right-hand side look similar to what is expected for planar films. The error bars are standard deviations from three runs with randomly positioned particles. For the shifts themselves, they are hardly discerned. They do become substantial for the ff ratios. The parameters of the simulation were $|n_{\text{Sph}}| = 100$ mPa s, $\tan \delta = 1$, $R_{\text{Sph}} = 10$ nm, and $\Delta x_{\text{S1}} = 2.5$ nm. Spheres were truncated at the bottom by 5%.

by Mindlin and is described in the book by Popov.^[63] Following Mindlin theory, the transverse stiffness of the contact is given as $\kappa_S = 2 G_c r_c$. G_c is an effective modulus, similar in value to the shear modulus. r_c is the contact radius, which in ref. [29] was calculated from Derjaguin–Müller–Toporov (DMT) theory.^[63] Following Dominik and Tielens,^[47,64] the bending stiffness is calculated as $\kappa_B = \kappa_S \cdot 2(r_c/R_{\text{Sph}})^2$.

After every LB step, the motion of the spheres is updated, applying the following steps:

- i. Calculate the forces, F_k , at the points where the links intersect the surface from Equation (13). The index k labels the links.
- ii. Calculate the total force along x , F_x , and the total torque about the z -axis, T_z . The torque is applied around the point of contact. The calculation amounts to a summation of forces for F_x and to a summation of $r_k \times F_k$ for the torque. r_k is the vector, which links the contact to the respective point.
- iii. Calculate the target amplitudes of translation along x as $u_{x,\text{target}} = F_x/\kappa_S$. Calculate the target amplitudes of rotation about z as $\Omega_{z,\text{target}} = T_z/(R_{\text{Sph}} \kappa_B)$.
- iv. Change the amplitudes of translation and rotation so that they come closer to the target. The approach must occur in small steps in order to avoid instabilities. Typically, the step width is 5% of the distance between the current amplitude and target amplitude.
- v. Calculate the velocities of the points at the surface from the updated values of u_x and Ω_z . Use those velocities for the bounce-back in the next LBM step.

In ref. [29], varied parameters were the modulus and the loss tangent of the contact stiffness, $|\kappa_S|$ and κ_S''/κ_S' . The comparison between simulation and experiment was based on the Df ratio, shown in the column to the right in Figure 27. The experimental data are shown as open squares. The different rows show simulations, where the contact stiffness as expected from Mindlin theory and DMT theory^[63] were multiplied by some numerical factor α_κ as indicated above the graphs to the left. The agreement is never perfect, but the agreement is better for α_κ between 0.01 and 0.04 (second and third row) than for the other choices. It can be safely stated that Mindlin theory and DMT theory overestimate the contact stiffness. There are different possible reasons, among them roughness, the presence of the liquid, and an overestimation of the force of adhesion used in the calculation of the contact radius with DMT theory.

7.3. Stationary Large Sphere Above the Resonator

The third application example is meant to illustrate the flexibility of FreqD-LBM. The calculation requires some further additions to the code, which may cause confusion to readers not actually interested in the surface forces apparatus. For that reason, the additions needed for this calculation were not uploaded to GitHub.

The combination of the QCM with the surface forces apparatus (SFA)^[65] is a long-standing target. The SFA approaches two cylinders to each other, the surfaces of which have been made to be atomically flat, using mica sheets glued to the rods. The distance between the surfaces is measured interferometri-

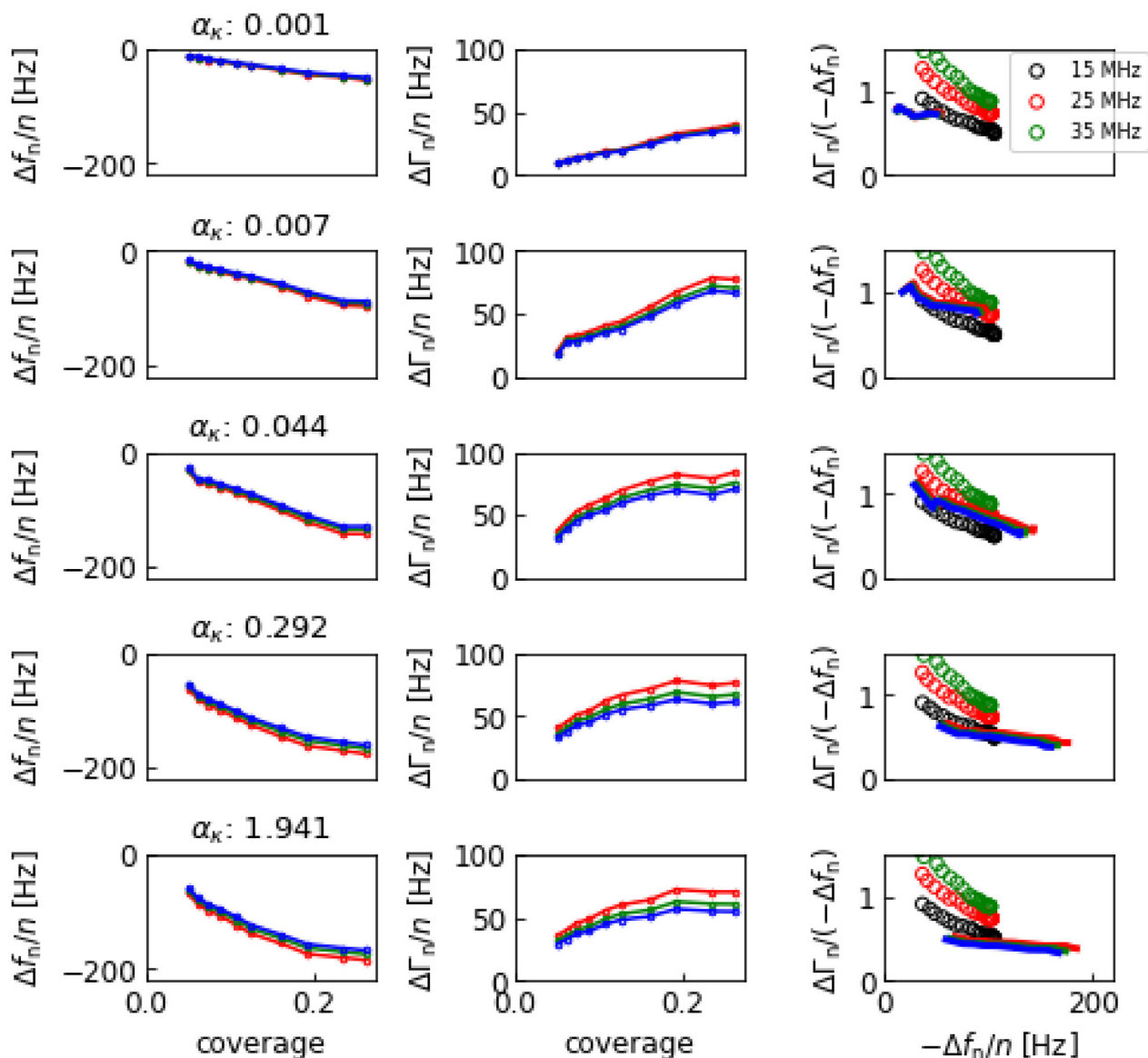


Figure 27. A simulation attempting to reproduce experiments on the adsorption of hard spheres to the resonator surface. The open symbols on the right-hand side are experimental data from ref. [10]. Parameters of the simulation were $R_{\text{Sph}} = 13 \text{ nm}$, $\Delta x_{\text{SI}} = R_{\text{Sph}}/3$, $\tan \delta = \kappa''/\kappa' = 0.3$. The modulus of the contact stiffness as calculated from DMT theory and Mindlin theory was multiplied with same factor α_{κ} . The rows show simulations with different values of α_{κ} . Adapted from ref. [29].

cally. In the original version, force-distance curves are obtained. The SFA today is often combined with measurements of the transverse forces obtained when translating one of the cylinders laterally.^[66,67]

Combination with the QCM would also make the high-frequency shear properties of the sample in the gap available. The combination requires the two cylinders to be replaced by the quartz resonator and a glass sphere. This entails compromises, but can be done.^[68,69] Also, an understanding is required of how a sample in the gap (such as a polymer brush) affects $\Delta f_n/n$ and $\Delta \Gamma_n/n$. Such an understanding requires a numerical simulation. A result of such a simulation is shown in **Figure 28**.

When approaching the sphere, the frequency increases first (solid lines). The change in bandwidth follows later (dashed lines)

and goes through a shallow minimum. The minimum is caused by the reflection of the wave at the sphere surface, which channels energy back into the resonator, thereby reducing the amount of energy radiated away from the resonator into the ambient medium. **Figure 28** is meant to be proof of feasibility. More detailed studies will have to, for instance, include a realistic segment density profile of the brush.

7.4. Possible Other Applications

Other problems to be addressed can be the following:

- i. Hydrodynamic spectroscopy as described in ref. [71] can be backed up with calculations of how rough surfaces af-

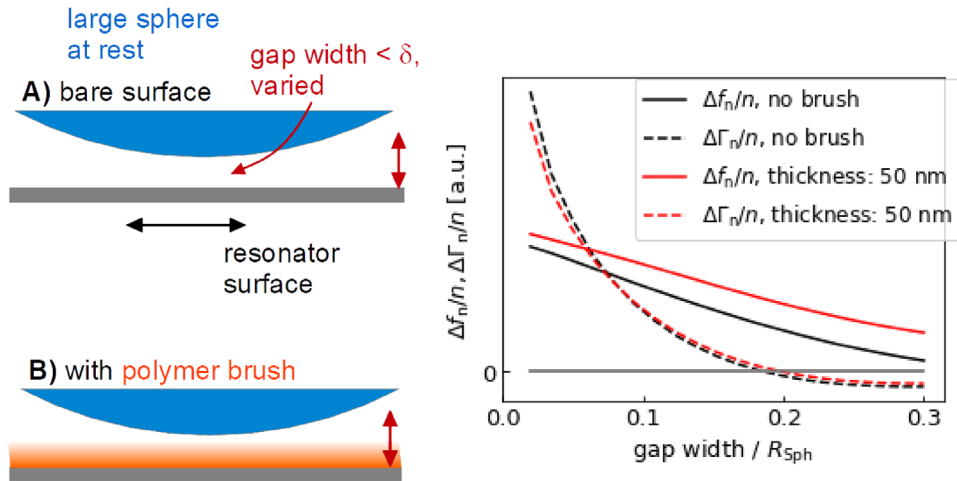


Figure 28. FreqD-LBM can predict $\Delta f_n/n$ and $\Delta \Gamma_n/n$ seen when a large, immobile sphere is approached from the top. Such experiments would aim to reproduce experiments, where a surface forces apparatus (SFA) is combined with a QCM. The cylinder typically used in the SFA must be replaced by a smooth sphere. The parameters of the simulation were $R_{Sph} = 1000$ nm, cell width = 200 nm, $\Delta x_{S1} = 30$ nm, $|\eta_{brush}| = 100$ mPa s, and $(\tan \delta)_{brush} = 1$. A box profile of the viscosity was assumed.

fect $\Delta f_n/n$ and $\Delta \Gamma_n/n$ without the need of simplifying assumptions.

- ii. Embedded objects can be nanobubbles or vesicles. The calculation of the forces at the surface will then involve the surface tension and the membrane elasticity, respectively.
- iii. It is straight-forward to calculate steady forces from the oscillatory flow field. These are caused by the nonlinear term in the Navier-Stokes equation, assuming weak nonlinearities. They lead to steady streaming.^[43,71,72]
- iv. Possibly, FreqD-LBM can be coupled with models which generate structures such as phase-field models for electrochemical applications.^[73]

8. Conclusions and Outlook

FreqD-LBM produces robust results for adsorbed particles, either soft or rigid. The code can run on an office PC.

There certainly is room for improvement. This firstly concerns other embedded objects, which might be nanobubbles or vesicles. Modeling vesicles would be particularly attractive, because this would allow to quantitatively understand the famous experiment by Keller and Kasemo^[9] (which have been repeated many times). Another goal for improvement is parallelization. In LBM, the collision step is often distributed to many GPUs. Further, it can be hoped that the condition of stationarity, which underlies the calculations in sections 4.1 and 4.2, can be extended to the entire simulation. A sparse matrix results. FreqD-LBM then may be much faster.

Rigorous proofs of correctness have only been provided for the plain shear wave and the plain compressional wave. A rigorous proof of correctness (not easily digested by the non-expert) was supplied by Shi and Sader for the homogeneous Newtonian liquid.^[23] Experts might have a second go to prove the correctness of FreqD-LBM including spatially variable viscoelasticity and density in more general terms.

The authors believe that research with the QCM has much to gain from an understanding of structured samples. Of course,

some samples are too complicated. For complicated samples, modeling based on the sets of $\{\Delta f_n/n\}$ and $\{\Delta \Gamma_n/n\}$ alone will not provide unique answers. Some interesting samples are not simple enough in that sense, but the QCM can be combined with other methods like atomic force microscopy to clarify structure. An understanding of those samples is in reach.

Appendix A: Boundary Condition at the Interface to the Bulk Liquid

The following section derives the boundary condition at the top in detail. The central result is the matrix in Equation (A59). Conceptually, the analysis building on the Fourier decomposition borrows from ref. [53]. Similar to the results from ref. [53] (treating shallow roughness), the boundary condition making use of the matrix from Equation (A59) is only valid in the limit of small amplitudes of normal motion. Otherwise, the different modes couple to each other. For that reason, the upper boundary of the simulation box must be located at some distance from the sample (section 5.2).

A.1. Local Impedance Boundary Condition in 2D

The following calculation employs the D2Q9 stencil. In the cases, where certain variables have fixed values, these values were often inserted, directly. This concerns $\rho \equiv 1$, $c_s^2 \equiv 1/3$, $\Delta x \equiv 1$, and $\Delta t \equiv 1$. The calculation assumes a Newtonian liquid on both sides of the boundary.

Bounce-back occurs as

$$\begin{aligned}
 h_7 &= h_5 = h_5 - c_{x,5} \frac{2\rho}{c_s^2} w_d u_x^T - c_{y,5} \frac{2\rho}{c_s^2} w_s u_y^T = h_5 \\
 &\quad - \frac{3 \cdot 2}{36} w_d u_x^T - \frac{3 \cdot 2}{9} w_s u_y^T \\
 &= h_5 - \frac{1}{6} u_x^T - \frac{2}{3} u_y^T h_8 = h_6 = h_6 - c_{x,6} \frac{2\rho}{c_s^2} w_d u_x^T - c_{y,6} \frac{2\rho}{c_s^2} w_s u_y^T \\
 &= h_6 + c_{x,6} \frac{3 \cdot 2}{36} u_x^T - \frac{3 \cdot 2}{9} w_s u_y^T = h_6 + \frac{1}{6} u_x^T - \frac{2}{3} u_y^T \\
 h_4 &= h_2 = h_2 - c_{y,2} \frac{2\rho}{c_s^2} w_s u_y^T = h_2 - \frac{3 \cdot 2}{9} w_s u_y^T = h_2 - \frac{2}{3} u_y^T \quad (A1)
 \end{aligned}$$

$w_5 = 1/9$ and $w_4 = 1/36$ are the weight factors. The superscript T denotes the top. Technically speaking, the populations (h) should also carry a superscript T, because they are evaluated at the top. The "T" was omitted for brevity. The stresses are

$$\begin{aligned}\sigma_{xy}^T &= c_{x,5} (h_5 + h_{\bar{5}}) + c_{x,6} (h_6 + h_{\bar{6}}) + c_{x,2} (h_2 + h_{\bar{2}}) \\ &= (h_5 + h_{\bar{5}}) - (h_6 + h_{\bar{6}}) + 0 (h_2 + h_{\bar{2}}) = 2 (h_5 - h_6) - \frac{1}{3} u_x^T\end{aligned}\quad (A2)$$

$$\begin{aligned}\sigma_{yy}^T &= c_{y,5} (h_5 + h_{\bar{5}}) + c_{y,6} (h_6 + h_{\bar{6}}) + c_{y,2} (h_2 + h_{\bar{2}}) \\ &= (h_5 + h_{\bar{5}}) + (h_6 + h_{\bar{6}}) + (h_2 + h_{\bar{2}}) = 2 (h_5 + h_6 + h_2) - 2u_y^T\end{aligned}$$

For convenience of notation, the terms containing populations are collected as

$$\begin{aligned}H_{xy} &= 2 (h_5 - h_6) \\ H_{yy} &= 2 (h_5 + h_6 + h_2)\end{aligned}\quad (A3)$$

With this shortened notation Equation (A2) turns into

$$\begin{aligned}\sigma_{xy}^T &= H_{xy} - \frac{1}{3} u_x^T \\ \sigma_{yy}^T &= H_{yy} - 2u_y^T\end{aligned}\quad (A4)$$

The stress as calculated from bounce-back is related to the velocity as

$$\begin{aligned}\sigma_{xy}^T &= Z_{liq} u_x^T \\ \sigma_{yy}^T &= Z_{comp} u_y^T\end{aligned}\quad (A5)$$

The impedance by definition is ratio of stress to velocity. $Z_{liq} = (G\rho)^{1/2} = (\omega\eta\rho)^{1/2}$ is the liquid's shear-wave impedance (a materials constant). $Z_{comp} = \rho c_s$ is the liquid's compressional-wave impedance (also a materials constant). Combining Equation (A5) with Equation (A4) leads to

$$\begin{aligned}Z_{liq} u_x^T &= H_{xy} - \frac{1}{3} u_x^T \\ Z_{comp} u_y^T &= H_{yy} - 2u_y^T\end{aligned}\quad (A6)$$

Solving for the velocities leads to

$$\begin{aligned}u_x^T &= \frac{H_{xy}}{Z_{liq} + \frac{1}{3}} \\ u_y^T &= \frac{H_{yy}}{Z_{comp} + 2}\end{aligned}\quad (A7)$$

For the sake of comparison with Equation (A29), we write Equation (A7) in matrix form as

$$\begin{pmatrix} u_x^T \\ u_y^T \end{pmatrix} = \begin{bmatrix} \frac{1}{(Z_{liq} + \frac{1}{3})} & 0 \\ 0 & \frac{1}{Z_{comp} + 2} \end{bmatrix} \begin{pmatrix} H_{xy} \\ H_{yy} \end{pmatrix}\quad (A8)$$

Inserting Equation (A8) into Equation (A1) completes the bounce-back.

A.2. Bounce-Back Condition Computed from the Analytical Solution in the Bulk

A.2.1. Fourier Decomposition of the Flow Field

One Fourier-decomposes the flow field and finds amplitudes $u_{x,q}$ and $u_{y,q}$ for a certain number of Fourier components (Figure A1). q takes the values

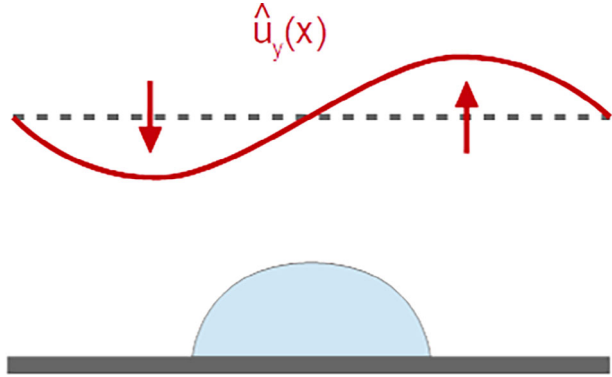


Figure A1. The algorithm matches the different Fourier components of u_x and u_y between the simulation box and the bulk. This box contains a hemisphere in the center (in blue). The sketch at the top shows the vertical component of the velocity for one selected Fourier component.

$$q = m \frac{\pi}{L} \quad m = -\frac{n_x}{2} \dots \frac{n_x}{2}\quad (A9)$$

L is the lateral size of the box.

The Fourier components of the populations h_i ($i = 0, \dots, 8$) pertaining to q are

$$h_{i,q} = \frac{1}{n_x} \sum_{j=0}^{n_x-1} \sum h_i(x_j) \exp(-iqx_j)\quad (A10)$$

The index j labels the nodes. The target is to find relations analogous to Equation (A7) and Equation (A8) for all Fourier-components. On the way, the amplitudes of the bulk flows must be determined.

The problem has three dynamical variables, which are the two velocities ($u_{x,q}$, $u_{y,q}$) and the pressure p_q . (The superscript T for the velocities at the Top was dropped for brevity). The flow pattern above the upper surface is of the form

$$\exp(i\omega t) \exp(-i(qx + ky))\quad (A11)$$

A.2.2. Evanescent and Propagating Modes

It will turn out, that there are two separate k 's for every in-plane wave vector q . There are two modes with separate eigenvectors, where an eigenvector is a tuple of velocities ($u_{x,q}$, $u_{y,q}$). Volume conservation implies

$$\frac{\partial u_{x,q}}{\partial x} + \frac{\partial u_{y,q}}{\partial y} = -iqu_{x,q} - iku_{y,q} = 0\quad (A12)$$

For incompressible flows, the Stokes law is

$$\rho \frac{\partial u_q}{\partial t} = \eta \nabla^2 u_q - \nabla p_q\quad (A13)$$

Volume conservation and the Stokes law spell out as

$$\begin{aligned}-iqu_{x,q} - iku_{y,q} &= 0 & a) \\ i\omega u_{x,q} &= -v(k^2 + q^2) u_{x,q} + iq \frac{p_q}{\rho} & b) \\ i\omega u_{y,q} &= -v(k^2 + q^2) u_{y,q} + ik \frac{p_q}{\rho} & c)\end{aligned}\quad (A14)$$

Written in matrix form (and with some signs reverted for convenience), this equation system turns into

$$\begin{bmatrix} iq & ik & 0 \\ i\omega + \nu(k^2 + q^2) & 0 & -iq \\ 0 & i\omega + \nu(k^2 + q^2) & -ik \end{bmatrix} \begin{pmatrix} u_{x,q} \\ u_{y,q} \\ p_q/\rho \end{pmatrix} = 0 \quad (\text{A15})$$

The determinant of must vanish, which implies

$$(iq)^2(i\omega + \nu(k^2 + q^2)) + (ik)^2(i\omega + \nu(k^2 + q^2)) = 0 \quad (\text{A16})$$

$$[q^2 + k^2][i\omega + \nu(k^2 + q^2)] = 0$$

Setting the first term in square brackets to zero yields the first mode, which we call “evanescent” (subscript “E”). k_E is given as

$$k_E = -i|q| \quad (\text{A17})$$

A comment to the sign: We write the y -dependence of the wave as $\exp(-iky)$ with $k = k' - ik''$ and $k'' > 0$. Written this way, k'' must be positive in order to let the wave decay towards $+\infty$. The root in Equation (A17) was chosen accordingly.

Setting the second square bracket in Equation (A16) to zero yields

$$k_P = -i\sqrt{q^2 + \frac{i\omega}{\nu}} = -ik_0\xi \quad (\text{A18})$$

$$k_0 = \sqrt{\frac{i\omega}{\nu}} = \frac{Z_{liq}}{\eta} \quad \xi = \frac{\sqrt{q^2 + k_0^2}}{k_0}$$

We call this mode “propagating” (subscript “P”, Figure A2). Again, the sign of the root was chosen such that the wave decays toward $+\infty$. k_0 is related to the penetration depth of the shear wave δ as $k_0 = (2i)^{1/2}/\delta$.

The case $q = 0$ must be treated separately. In this case, the boundary condition implies the absence of an evanescent mode. The “propagating mode” actually is evanescent with $k = -ik_0$. In this case $u_y \equiv 0$ and bounce-back occurs following Equation (A7) and A8. The following equations pertain to $q \neq 0$.

Volume conservation (Equation A14) leads to

$$u_{y,q,E} = -\frac{q}{k_E} u_{x,q,E} = -\frac{q}{-i|q|} u_{x,q,E} = -\text{sgn}(q) i u_{x,q,E} \quad (\text{A19})$$

$$u_{y,q,P} = -\frac{q}{k_P} u_{x,q,P} = -\frac{q}{-ik_0\xi} u_{x,q,P} = -i\frac{q}{k_0\xi} u_{x,q,P}$$

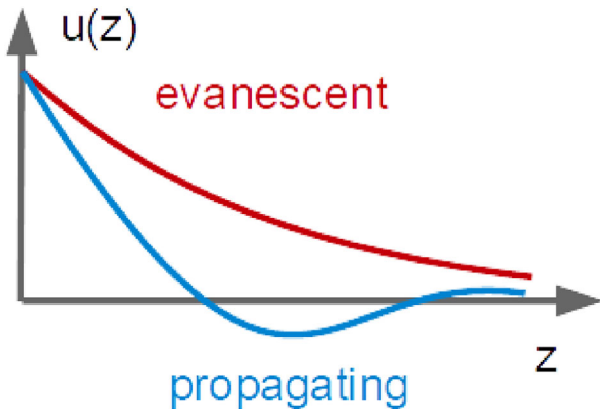


Figure A2. The evanescent mode decays exponentially, while the propagating mode has an oscillatory component propagating towards $+\nu$. Both modes eventually decay.

The velocities along x and y are

$$u_{x,q} = u_{x,q,E} + u_{x,q,P} \quad (\text{A20})$$

$$u_{y,q} = u_{y,q,E} + u_{y,q,P} = -\text{sgn}(q) i u_{x,q,E} - i\frac{q}{k_0\xi} u_{x,q,P}$$

In matrix form, this reads as

$$\begin{pmatrix} u_{x,q} \\ u_{y,q} \end{pmatrix} = \begin{bmatrix} 1 & 1 \\ -\text{sgn}(q) i & -i\frac{q}{k_0\xi} \end{bmatrix} \begin{pmatrix} u_{x,q,E} \\ u_{x,q,P} \end{pmatrix} = [A] \begin{pmatrix} u_{x,q,E} \\ u_{x,q,P} \end{pmatrix} \quad (\text{A21})$$

A.2.3. Calculation of the Stress

For the pressure, one finds (Equation A14b).

$$\frac{p_{q,E}}{\rho} = \frac{i\omega + \nu(k_E^2 + q^2)}{iq} u_{x,q,E} = \frac{i\omega + \nu(-q^2 + q^2)}{iq} u_{x,q,E} = \frac{\omega}{q} u_{x,q,E}$$

$$\frac{p_{q,P}}{\rho} = \frac{i\omega + \nu(k_P^2 + q^2)}{iq} u_{x,q,P} = -\frac{i\omega + \nu\left(\left(i\sqrt{q^2 + i\omega/\nu}\right)^2 + q^2\right)}{iq} u_{x,q,P}$$

$$= -\frac{i\omega + \nu(-q^2 - i\omega/\nu + q^2)}{iq} u_{x,q,P} = 0 \quad (\text{A22})$$

The stresses are

$$\sigma_{xy,q} = -\eta \left(\frac{\partial}{\partial x} u_{y,q} + \frac{\partial}{\partial y} u_{x,q} \right)$$

$$= -\eta \left(-iqu_{y,q,E} - iqu_{y,q,P} - ik_E u_{x,q,E} - ik_P u_{x,q,P} \right)$$

$$= -\eta \left((-iq) (-\text{sgn}(q) i u_{x,q,E}) + (-iq) \left(-i\frac{q}{k_0\xi} i u_{x,q,P} \right) \right)$$

$$= -\eta \left(+(-i) (-\text{sgn}(q) iq) u_{x,q,E} + (-i) (-ik_0\xi) u_{x,q,P} \right)$$

$$= -\eta \left(-\text{sgn}(q) qu_{x,q,E} - \frac{q^2}{k_0\xi} u_{x,q,P} - \text{sgn}(q) qu_{x,q,E} - k_0\xi u_{x,q,P} \right)$$

$$= -\eta \left(-2\text{sgn}(q) qu_{x,q,E} - \left(\frac{q^2}{k_0\xi} + k_0\xi \right) u_{x,q,P} \right)$$

$$\sigma_{yy,q} = p_{q,E} + p_{q,P} = \frac{\rho\omega}{q} u_{x,q,E} = \frac{\eta\omega}{\nu q} u_{x,q,E} = -i\eta \frac{k_0^2}{q} u_{x,q,E} \quad (\text{A23})$$

The minus sign before η is needed because the stress propagates upwards. A negative gradient in velocity produces a positive shear stress. Replacing η by Z_{liq}/k_0 results in

$$\begin{pmatrix} \sigma_{xy,q} \\ \sigma_{yy,q} \end{pmatrix} = Z_{liq} \begin{bmatrix} \text{sgn}(q) \frac{2q}{k_0} & \frac{q^2}{k_0\xi} + \xi \\ -\frac{ik_0}{q} & 0 \end{bmatrix} \begin{pmatrix} u_{x,q,E} \\ u_{x,q,P} \end{pmatrix} = [B_q] \begin{pmatrix} u_{x,q,E} \\ u_{x,q,P} \end{pmatrix} \quad (\text{A24})$$

Combined with Equation (A21), this reads as

$$\begin{pmatrix} \sigma_{xy,q} \\ \sigma_{yy,q} \end{pmatrix} = [B_q] \begin{pmatrix} u_{x,q,E} \\ u_{x,q,P} \end{pmatrix} = [B_q] [A_q^{-1}] \begin{pmatrix} u_{x,q} \\ u_{y,q} \end{pmatrix} \quad (\text{A25})$$

This relation replaces Equation (A5) from section 9.1. The product $[B][A^{-1}]$ is

$$[B_q] [A_q^{-1}] = Z_{liq} \begin{bmatrix} \frac{\text{sgn}(q) (-q^2 + k_0^2 \xi^2)}{k_0 (-q + k_0 \text{sgn}(q) \xi)} & -\frac{i (q^2 - 2k_0 q \text{sgn}(q) \xi + k_0^2 \xi^2)}{k_0 (-q + k_0 \text{sgn}(q) \xi)} \\ -\frac{ik_0}{q - k_0 \text{sgn}(q) \xi} & -\frac{k_0^2 \xi}{q^2 - k_0 q \text{sgn}(q) \xi} \end{bmatrix} \quad (\text{A26})$$

A.2.4. Bounce-Back in q -Space

The bounce-back condition is the same as in Equation (A1), now for each Fourier component, separately. In matrix form Equation (A4) is

$$\begin{pmatrix} \sigma_{xy,q}^T \\ \sigma_{xy,q}^T \end{pmatrix} = \begin{pmatrix} H_{xy,q} \\ H_{yy,q} \end{pmatrix} - \begin{bmatrix} 1/3 & 0 \\ 0 & 2 \end{bmatrix} \begin{pmatrix} u_{x,q}^T \\ u_{y,q}^T \end{pmatrix} = \begin{pmatrix} H_{xy,q} \\ H_{yy,q} \end{pmatrix} - [D] \begin{pmatrix} u_{x,q}^T \\ u_{y,q}^T \end{pmatrix} \quad (\text{A27})$$

Combining Equation (A27) with Equation (A25) yields

$$[B_q] [A_q]^{-1} \begin{pmatrix} u_{x,q}^T \\ u_{y,q}^T \end{pmatrix} = \begin{pmatrix} H_{xy,q} \\ H_{yy,q} \end{pmatrix} - [D] \begin{pmatrix} u_{x,q}^T \\ u_{y,q}^T \end{pmatrix} \quad (\text{A28})$$

Solved for the velocities, Equation (A28) reads as

$$\begin{pmatrix} u_{x,q}^T \\ u_{y,q}^T \end{pmatrix} = ([B_q] [A_q]^{-1} + [D])^{-1} \begin{pmatrix} H_{xy,q} \\ H_{yy,q} \end{pmatrix} \quad (\text{A29})$$

This relation replaces Equation (A8) from section 9.1.

Equation (A29) solves the problem. Inserted into Equation (A1) (for each Fourier component separately), it prescribes the bounce-back algorithm. The matrix on the right-hand side in Equation (A29) is

$$[F_q] = ([B_q] [A_q]^{-1} + [D])^{-1} = \frac{1}{E} \begin{bmatrix} 2 - \frac{k_0^2 \xi Z_{liq}}{q^2 - k_0 q \text{sgn}(q) \xi} & \frac{i (q^2 - 2k_0 q \text{sgn}(q) \xi + k_0^2 \xi^2) Z_{liq}}{k_0 (-q + k_0 \text{sgn}(q) \xi)} \\ \frac{ik_0 Z_{liq}}{(q - k_0 \text{sgn}(q) \xi)} & \frac{1}{3} + \frac{\text{sgn}(q) (-q^2 + k_0^2 \xi^2) Z_{liq}}{k_0 (-q + k_0 \text{sgn}(q) \xi)} \end{bmatrix} \\ E = \frac{(q^2 - 2k_0 q \text{sgn}(q) \xi + k_0^2 \xi^2) Z_{liq}^2}{(q - k_0 \text{sgn}(q) \xi) (-q + k_0 \text{sgn}(q) \xi)} + \left(2 - \frac{k_0^2 \xi Z_{liq}}{q^2 - k_0 q \text{sgn}(q) \xi} \right) \\ \times \left(\frac{1}{3} + \frac{\text{sgn}(q) (-q^2 + k_0^2 \xi^2) Z_{liq}}{k_0 (-q + k_0 \text{sgn}(q) \xi)} \right) \quad (\text{A30})$$

In the limit of $q \rightarrow 0$ one has $\xi \rightarrow 1$ and

$$[F_q] \xrightarrow{q \rightarrow 0} \begin{bmatrix} \frac{1}{Z_{liq} + 1/3} & 0 \\ 0 & 0 \end{bmatrix} \quad (\text{A31})$$

A.3. Local Impedance Boundary Condition in 3D

The structure of the equations governing bounce-back is the same as in section 9.1. The equations only need to be adapted to the D3Q19 scheme

(Figure 2). Bounce-back occurs as

$$h_8 = h_7 = h_7 - c_{x,7} \frac{2\rho}{c_s^2} w_d u_x^T - c_{y,7} \frac{2\rho}{c_s^2} w_d u_y^T = h_7 - \frac{3 \cdot 2}{36} u_x^T - \frac{3 \cdot 2}{36} u_y^T \\ = h_7 - \frac{1}{6} u_x^T - \frac{1}{6} u_y^T h_{13} = h_{\bar{1}4} = h_{14} - c_{x,14} \frac{2\rho}{c_s^2} w_d u_x^T - c_{y,14} \frac{2\rho}{c_s^2} w_d u_y^T \\ = h_{14} + \frac{3 \cdot 2}{36} u_x^T - \frac{3 \cdot 2}{36} u_y^T = h_{14} + \frac{1}{6} u_x^T - \frac{1}{6} u_y^T h_{12} = h_{\bar{1}1} \\ = h_{11} - c_{x,11} \frac{2\rho}{c_s^2} w_d u_x^T - c_{z,11} \frac{2\rho}{c_s^2} w_d u_z^T = h_{11} + \frac{3 \cdot 2}{36} u_x^T - \frac{3 \cdot 2}{36} u_y^T \\ = h_{11} - \frac{1}{6} u_z^T - \frac{1}{6} u_y^T h_{18} = h_{17} = h_{17} - c_{x,17} \frac{2\rho}{c_s^2} w_d u_x^T - c_{z,17} \frac{2\rho}{c_s^2} w_d u_z^T \\ = h_{17} + \frac{3 \cdot 2}{36} u_x^T - \frac{3 \cdot 2}{36} u_y^T = h_{17} + \frac{1}{6} u_z^T - \frac{1}{6} u_y^T \\ h_4 = h_3 = h_3 - c_{y,3} \frac{2\rho}{c_s^2} w_s u_y^T = h_3 - \frac{3 \cdot 2}{18} u_y^T = h_3 - \frac{1}{3} u_y^T \quad (\text{A32})$$

$w_s = 1/18$ and $w_d = 1/36$ are the weight factors. w_s differs between the D2Q9 scheme and the D3Q19-scheme. The stresses are

$$\sigma_{xy} = c_{x,7} (h_7 + h_{\bar{7}}) + c_{x,14} (h_{14} + h_{\bar{1}4}) = [2 (h_7 - h_{14})] - \frac{1}{3} u_z^T \\ = H_{xy} - \frac{1}{3} u_z^T \sigma_{yy} = c_{y,7} (h_7 + h_{\bar{7}}) + c_{y,14} (h_{14} + h_{\bar{1}4}) + c_{y,14} (h_3 + h_{\bar{3}}) \\ = [2 (h_7 + h_{14} + h_{11} + h_{17} + h_3)] - u_y^T = H_{yy} - u_y^T \\ \sigma_{zy} = c_{x,11} (h_{11} + h_{\bar{1}1}) + c_{x,17} (h_{17} + h_{\bar{1}7}) = [2 (h_{11} - h_{17})] - \frac{1}{3} u_z^T \\ = H_{zy} - \frac{1}{3} u_z^T \quad (\text{A33})$$

For convenience of notation, the terms containing populations have been collected as

$$H_{xy} = 2 (h_7 - h_{14}) \\ H_{yy} = 2 (h_7 + h_{14} + h_{11} + h_{17} + h_3) \\ H_{zy} = 2 (h_{11} - h_{17}) \quad (\text{A34})$$

The stress as calculated from bounce-back is related to the velocity as

$$\sigma_{xy}^T = Z_{liq} u_x^T \\ \sigma_{yy}^T = Z_{comp} u_y^T \\ \sigma_{zy}^T = Z_{liq} u_z^T \quad (\text{A35})$$

$Z_{liq} = (G\rho)^{1/2} = (i\omega\eta\rho)^{1/2}$ is the liquid's shear-wave impedance (a materials constant). $Z_{comp} = \rho c_s$ is the liquid's compressional-wave impedance. Combining Equation (A35) with Equation (A33) results in

$$Z_{liq} u_x^T = H_{xy} - \frac{1}{3} u_z^T \\ Z_{comp} u_y^T = H_{yy} - u_y^T \\ Z_{liq} u_z^T = H_{zy} - \frac{1}{3} u_z^T \quad (\text{A36})$$

Solving for the velocities leads to

$$\begin{aligned} u_x^T &= \frac{H_{xy}}{Z_{liq} + 1/3} \\ u_y^T &= \frac{H_{yy}}{Z_{comp} + 1} \\ u_z^T &= \frac{H_{zy}}{Z_{liq} + 1/3} \end{aligned} \quad (\text{A37})$$

In matrix form, Equation (A37) is

$$\begin{pmatrix} u_x^T \\ u_y^T \\ u_z^T \end{pmatrix} = \begin{bmatrix} \frac{1}{(Z_{liq} + \frac{1}{3})} & 0 & 0 \\ 0 & \frac{1}{Z_{comp} + 1} & 0 \\ 0 & 0 & \frac{1}{(Z_{liq} + \frac{1}{3})} \end{bmatrix} \begin{pmatrix} H_{xy} \\ H_{yy} \\ H_{zy} \end{pmatrix} = [F] \begin{pmatrix} H_{xy} \\ H_{yy} \end{pmatrix} \quad (\text{A38})$$

A.4. Bounce-Back Condition Computed from the Analytical Solution in the Bulk in 3D

To prepare for the algebra below we rewrite Equation (A36) as

$$\begin{pmatrix} \sigma_{xy}^T \\ \sigma_{yy}^T \\ \sigma_{zy}^T \end{pmatrix} = [Z] \begin{pmatrix} u_x^T \\ u_y^T \\ u_z^T \end{pmatrix} = \begin{pmatrix} H_{xy} \\ H_{yy} \\ H_{zy} \end{pmatrix} - [D] \begin{pmatrix} u_x^T \\ u_y^T \\ u_z^T \end{pmatrix} \quad (\text{A39})$$

or, in more compact form

$$\sigma = [Z] \mathbf{u}^T = \mathbf{H} - [D] \mathbf{u}^T \quad (\text{A40})$$

where the matrices $[Z]$ and $[D]$ are

$$[Z] = \begin{bmatrix} Z_{liq} & 0 & 0 \\ 0 & Z_{comp} & 0 \\ 0 & 0 & Z_{liq} \end{bmatrix} \quad [D] = \begin{bmatrix} 1/3 & 0 & 0 \\ 0 & 1 & 0 \\ 0 & 0 & 1/3 \end{bmatrix} \quad (\text{A41})$$

Stresses and velocities are related by an impedance matrix $[Z]$. Solving Equation (A40) for \mathbf{u}^T leads to

$$\mathbf{u}^T = ([Z] + [D])^{-1} \mathbf{H} = [F] \mathbf{H} \quad (\text{A42})$$

where the matrix $[F]$ is given in Equation (A38).

This paragraph briefly outlines the later steps in prose. \mathbf{u}^T and \mathbf{H} are replaced by Fourier-components \mathbf{u}_q^T and \mathbf{H}_q . Subsequently, the coordinate system is rotated, using the rotation matrix from Equation (A45) (Figure A3). Parameters in the rotated coordinate system are given a hat ($\mathbf{H}_q \rightarrow \hat{\mathbf{H}}_q$, $\mathbf{u}_q \rightarrow \hat{\mathbf{u}}_q$). $[Z]$ and $[F]$ are replaced by the matrices $[\hat{Z}_q]$ and $[\hat{F}_q]$ for each Fourier component. $\hat{\mathbf{u}}_q$ as calculated from $\hat{\mathbf{H}}_q$ using $[\hat{F}_q]$. $[\hat{F}_q]$ is the central outcome of the calculation (Equation A59). The rotation is reverted to obtain \mathbf{u} from $\hat{\mathbf{u}}_q$. The inverse Fourier transform yields \mathbf{u} from \mathbf{u}_q . The velocities \mathbf{u} inserted into the bounce-back step from Equation (A32) solve the problem.

We proceed with the algebra in detail. The function $\mathbf{H}(x,z)$ turns into $\mathbf{H}_q(q_x, q_z)$. The tuple (q_x, q_z) is an in-plane wave vector. The different Fourier components are treated separately. q_x and q_z take the values

$$\begin{aligned} q_{x,mx} &= m_x \frac{2\pi}{L} & q_{z,mz} &= m_z \frac{2\pi}{L} \\ m_x &= -\frac{n_x}{2} \dots \frac{n_x}{2}, & m_z &= -\frac{n_x}{2} \dots \frac{n_x}{2} \end{aligned} \quad (\text{A43})$$

L is the lateral size of the quadratic box.

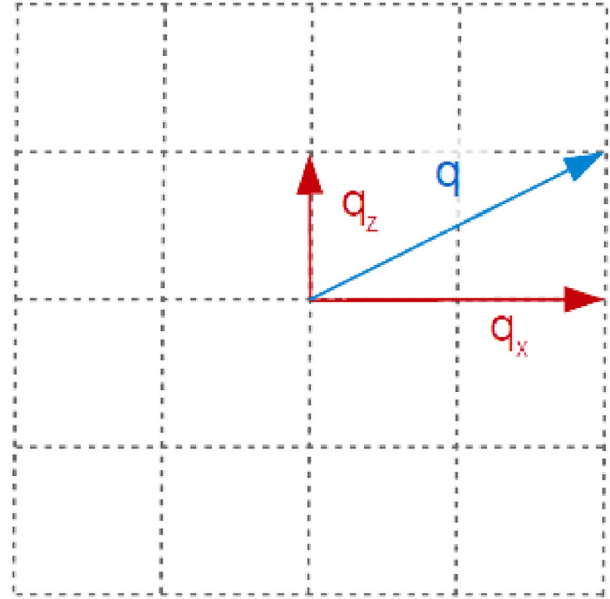


Figure A3. For each pair (q_x, q_z) , the coordinate system is rotated such that the spatial variability of the velocities occurs along x , only. Along the rotated z coordinate, the flow field is constant.

The calculation simplifies, if the coordinates are rotated such that $q_z = 0$ after the rotation (Figure A3). The rotation occurs as

$$\begin{pmatrix} \hat{u}_{x,q} \\ \hat{u}_{y,q} \\ \hat{u}_{z,q} \end{pmatrix} = [R_q] \begin{pmatrix} u_{x,q} \\ u_{y,q} \\ u_{z,q} \end{pmatrix} \quad (\text{A44})$$

where the rotation matrix, $[R]$, is given as

$$[R_q] = \begin{bmatrix} \cos(\varphi) & 0 & \sin(\varphi) \\ 0 & 1 & 0 \\ -\sin(\varphi) & 0 & \cos(\varphi) \end{bmatrix} \quad \text{with } \varphi = \arctan \frac{q_z}{q_x} \quad (\text{A45})$$

The role of q in section 9.2 is taken by the vector sum of q_x and q_z . The length of this vector is

$$q = (q_x^2 + q_z^2)^{1/2} \quad (\text{A46})$$

After Fourier transformation and rotation, Equation (A42) reads as

$$\begin{pmatrix} \hat{u}_{x,q}^T \\ \hat{u}_{y,q}^T \\ \hat{u}_{z,q}^T \end{pmatrix} = ([\hat{Z}_q] + [D])^{-1} \begin{pmatrix} \hat{H}_{xy,q} \\ \hat{H}_{yy,q} \\ \hat{H}_{zy,q} \end{pmatrix} = [\hat{F}_q] \begin{pmatrix} \hat{H}_{xy,q} \\ \hat{H}_{yy,q} \\ \hat{H}_{zy,q} \end{pmatrix} \quad (\text{A47})$$

The matrix $[D]$ has no index q , because it is the same for all Fourier components (always given by Equation A41). In 3D, Equation (A15) turns into

$$\begin{bmatrix} iq & ik & 0 & 0 \\ i\omega + \nu(k^2 + q^2) & 0 & 0 & -iq \\ 0 & i\omega + \nu(k^2 + q^2) & 0 & -ik \\ 0 & 0 & i\omega + \nu(k^2 + q^2) & 0 \end{bmatrix}$$

$$\times \begin{pmatrix} \hat{u}_{x,q} \\ \hat{u}_{y,q} \\ \hat{u}_{z,q} \\ \hat{p}_q/\rho \end{pmatrix} = 0 \quad (\text{A48})$$

Row 4 of the matrix contains only one element. (That was the purpose of the rotation.) This matrix element must be zero, individually. For $\hat{u}_{z,q}$, there is only one k-vector, $k_{[z]}$, given as

$$\begin{aligned} k_{[z]} &= -i\sqrt{q^2 + \frac{i\omega}{v}} = -ik_0\xi \\ k_0 &= \sqrt{\frac{i\omega}{v}\xi} = \frac{\sqrt{q^2 + k_0^2}}{k_0} \end{aligned} \quad (\text{A49})$$

Clearly, $k_{[z]}$ is the same as k_p from Equation (A18), but it was still given a different name to avoid confusion. Square brackets are used in the subscript to indicate that $k_{[z]}$ is not the z-component of some wave vector. $k_{[z]}$ is wavevector along the surface normal pertaining to $\hat{u}_{z,q}$.

Turning to the rotated xy-plane, the motion along \hat{x} is coupled to the motion along y (that is, along the surface normal). That is so, because the interface is dynamically corrugated along \hat{x} . (It is not corrugated along \hat{z} after coordinate rotation.) Removing the motion along \hat{z} from Equation (A48) leads to the following, smaller equation system:

$$\begin{bmatrix} iq & ik & 0 \\ i\omega + v(k^2 + q^2) & 0 & -iq \\ 0 & i\omega + v(k^2 + q^2) & -ik \end{bmatrix} \begin{pmatrix} \hat{u}_{x,q} \\ \hat{u}_{y,q} \\ \hat{p}_q/\rho \end{pmatrix} = 0 \quad (\text{A50})$$

This equation system is the same as in Equation (A15) and the following equations in part repeat section 9.2 for that reason. We still repeat most equations in full length for the sake of comprehensiveness.

The matrix from Equation (A21) turns into

$$\begin{pmatrix} \hat{u}_{x,q} \\ \hat{u}_{y,q} \\ \hat{u}_{z,q} \end{pmatrix} = \begin{bmatrix} 1 & 1 & 0 \\ -\text{sgn}(q) & i & -i\frac{q}{k_0\xi} \\ 0 & 0 & 1 \end{bmatrix} \begin{pmatrix} \hat{u}_{x,q,E} \\ \hat{u}_{x,q,P} \\ \hat{u}_{z,q} \end{pmatrix} = [\hat{A}_q] \begin{pmatrix} \hat{u}_{x,q,E} \\ \hat{u}_{x,q,P} \\ \hat{u}_{z,q} \end{pmatrix} \quad (\text{A51})$$

Equation (A23) turns into

$$\begin{aligned} \hat{\sigma}_{xy,q} &= -\eta \left(\frac{\partial}{\partial x} \hat{u}_{y,q} + \frac{\partial}{\partial y} \hat{u}_{x,q} \right) \\ &= -\eta \left(-iq\hat{u}_{y,q,E} - iq\hat{u}_{y,q,P} - ik_E\hat{u}_{x,q,E} - ik_P\hat{u}_{x,q,P} \right) \\ &= -\eta \left((-iq) (-\text{sgn}(q) i\hat{u}_{x,q,E}) + (-iq) \left(-i\frac{q}{k_0\xi} i\hat{u}_{x,q,P} \right) \right. \\ &\quad \left. + (-i(-\text{sgn}(q) iq)) \hat{u}_{x,q,E} + (-i(-ik_0\xi)) \hat{u}_{x,q,P} \right) \\ &= -\eta \left(-\text{sgn}(q) q\hat{u}_{x,q,E} - \frac{q^2}{k_0\xi} \hat{u}_{x,q,P} - \text{sgn}(q) q\hat{u}_{x,q,E} - k_0\xi\hat{u}_{x,q,P} \right) \\ &= -\eta \left(-2\text{sgn}(q) q\hat{u}_{x,q,E} - \left(\frac{q^2}{k_0\xi} + k_0\xi \right) \hat{u}_{x,q,P} \right) \\ \hat{\sigma}_{yy,q} &= \hat{p}_{E,q} + \hat{p}_{P,q} = \frac{\rho\omega}{q} \hat{u}_{x,q,E} = \frac{\eta\omega}{vq} \hat{u}_{x,q,E} = -i\eta \frac{k_0^2}{q} \hat{u}_{x,q,E} \\ \hat{\sigma}_{zy} &= -\eta \left(\frac{\partial}{\partial z} \hat{u}_{y,q} + \frac{\partial}{\partial y} \hat{u}_{z,q} \right) = -\eta (-ik_{[z]}) \hat{u}_{z,q} \\ &= -\eta (-i(-ik_0\xi)) \hat{u}_{z,q} = -\eta (-k_0\xi) \hat{u}_{z,q} \end{aligned} \quad (\text{A52})$$

Equation (A24) turns into

$$\begin{pmatrix} \hat{\sigma}_{xy,q} \\ \hat{\sigma}_{yy,q} \\ \hat{\sigma}_{zy,q} \end{pmatrix} = Z_{liq} \begin{bmatrix} \text{sgn}(q) \frac{2q}{k_0} & \frac{q^2}{k_0^2\xi} + \xi & 0 \\ -ik_0 & 0 & 0 \\ 0 & 0 & \xi \end{bmatrix} \begin{pmatrix} \hat{u}_{x,q,E} \\ \hat{u}_{x,q,P} \\ \hat{u}_{z,q} \end{pmatrix} = [B] \begin{pmatrix} \hat{u}_{x,q,E} \\ \hat{u}_{x,q,P} \\ \hat{u}_{z,q} \end{pmatrix} \quad (\text{A53})$$

Combined with Equation (A51), this reads as

$$\begin{pmatrix} \hat{\sigma}_{xy,q} \\ \hat{\sigma}_{yy,q} \\ \hat{\sigma}_{zy,q} \end{pmatrix} = [\hat{B}_q] \begin{pmatrix} \hat{u}_{x,q,E} \\ \hat{u}_{x,q,P} \\ \hat{u}_{z,q} \end{pmatrix} = [\hat{B}_q] [\hat{A}_q]^{-1} \begin{pmatrix} \hat{u}_{x,q} \\ \hat{u}_{y,q} \\ \hat{u}_{z,q} \end{pmatrix} \quad (\text{A54})$$

This relation replaces Equation (A5) from section 9.1. The product $[B][A^{-1}]$ is

$$\begin{aligned} [\hat{Z}_q] &= [\hat{B}_q] [\hat{A}_q]^{-1} \\ &= Z_{liq} \begin{bmatrix} \text{sgn}(q) \frac{(-q^2 + k_0^2\xi^2)}{k_0(-q + k_0\text{sgn}(q)\xi)} & \frac{i(q^2 - 2k_0q\text{sgn}(q)\xi + k_0^2\xi^2)}{k_0(-q + k_0\text{sgn}(q)\xi)} & 0 \\ -\frac{ik_0}{q - k_0\text{sgn}(q)\xi} & -\frac{k_0^2\xi}{q^2 - k_0q\text{sgn}(q)\xi} & 0 \\ 0 & 0 & \xi \end{bmatrix} \end{aligned} \quad (\text{A55})$$

Equation (A27) turns into

$$\begin{pmatrix} \hat{\sigma}_{xy,q}^T \\ \hat{\sigma}_{yy,q}^T \\ \hat{\sigma}_{zy,q}^T \end{pmatrix} = \begin{pmatrix} \hat{H}_{xy,q} \\ \hat{H}_{yy,q} \\ \hat{H}_{zy,q} \end{pmatrix} - \begin{bmatrix} 1/3 & 0 & 0 \\ 0 & 1 & 0 \\ 0 & 0 & 1/3 \end{bmatrix} \begin{pmatrix} \hat{u}_{x,q}^T \\ \hat{u}_{y,q}^T \\ \hat{u}_{z,q}^T \end{pmatrix} = \begin{pmatrix} \hat{H}_{xy,q} \\ \hat{H}_{yy,q} \\ \hat{H}_{zy,q} \end{pmatrix} - [D] \begin{pmatrix} \hat{u}_{x,q}^T \\ \hat{u}_{y,q}^T \\ \hat{u}_{z,q}^T \end{pmatrix} \quad (\text{A56})$$

Combining Equation (A56) with Equation (A54) yields

$$[\hat{Z}_q] \begin{pmatrix} \hat{u}_{x,q}^T \\ \hat{u}_{y,q}^T \\ \hat{u}_{z,q}^T \end{pmatrix} = \begin{pmatrix} \hat{H}_{xy} \\ \hat{H}_{yy} \\ \hat{H}_{zy} \end{pmatrix} - [D] \begin{pmatrix} \hat{u}_{x,q}^T \\ \hat{u}_{y,q}^T \\ \hat{u}_{z,q}^T \end{pmatrix} \quad (\text{A57})$$

Solved for the velocities, Equation (A28) reads as

$$\begin{pmatrix} \hat{u}_{x,q}^T \\ \hat{u}_{y,q}^T \\ \hat{u}_{z,q}^T \end{pmatrix} = ([\hat{Z}_q] + [D])^{-1} \begin{pmatrix} \hat{H}_{xy} \\ \hat{H}_{yy} \\ \hat{H}_{zy} \end{pmatrix} \quad (\text{A58})$$

This relation replaces Equation (A8) from section 9.1. The matrix on the right-hand side in Equation (A58) is

$$\begin{aligned} [\hat{F}_q] &= ([\hat{Z}_q] + [D])^{-1} \\ &= \frac{1}{E} \begin{bmatrix} 1 - \frac{k_0^2\xi Z_{liq}}{q^2 - k_0q\text{sgn}(q)\xi} & \frac{i(q^2 - 2k_0q\text{sgn}(q)k_0^2\xi^2)Z_{liq}}{k_0(-q + k_0\text{sgn}(q)\xi)} & 0 \\ \frac{ik_0 Z_{liq}}{(q - k_0\text{sgn}(q)\xi)} & \frac{1}{3} + \frac{\text{sgn}(q)(-q^2 + k_0^2\xi^2)Z_{liq}}{k_0(-q + k_0\text{sgn}(q)\xi)} & 0 \\ 0 & 0 & \frac{1}{\frac{1}{3} + \xi Z_{liq}} \end{bmatrix} \end{aligned}$$

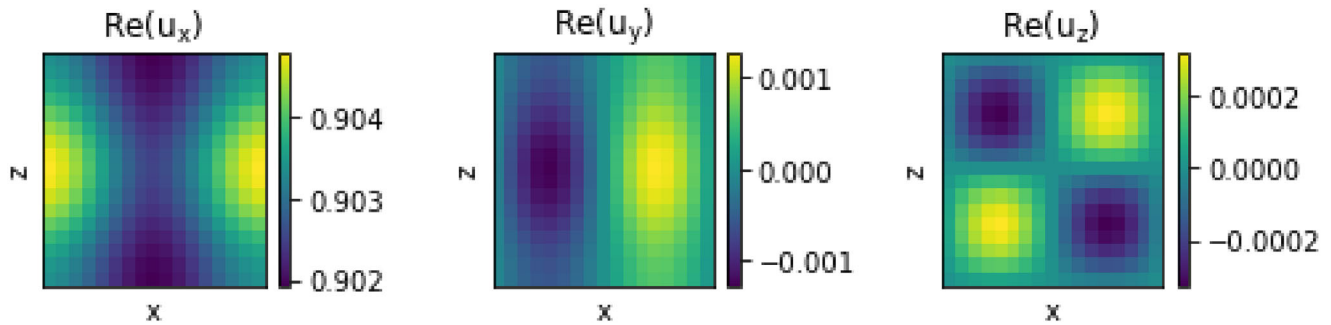


Figure A4. Real parts of the velocities at the top boundary calculated with Equation (A32) and Equation (A59). The box contained one particle in the center.

$$E = \frac{(q^2 - 2k_0 q \operatorname{sgn}(q) \xi + k_0^2 \xi^2) Z_{liq}^2}{(q - k_0 \operatorname{sgn}(q) \xi)(-q + k_0 \operatorname{sgn}(q) \xi)} + \left(1 - \frac{k_0^2 \xi Z_{liq}}{q^2 - k_0 q \operatorname{sgn}(q) \xi} \right) \left(\frac{1}{3} + \frac{\operatorname{sgn}(q)(-q^2 + k_0^2 \xi^2) Z_{liq}}{k_0(-q + k_0 \operatorname{sgn}(q) \xi)} \right) \quad (\text{A59})$$

In the limit of $q \rightarrow 0$ one has $\xi \rightarrow 1$ and

$$[\hat{F}_q] \xrightarrow{q \rightarrow 0} \begin{bmatrix} \frac{1}{Z_{liq} + 1/3} & 0 & 0 \\ 0 & 0 & 0 \\ 0 & 0 & \frac{1}{Z_{liq} + 1/3} \end{bmatrix} \quad (\text{A60})$$

At this point, the rotation of the coordinate system must be reversed, which is achieved by

$$[F_q] = [R]^{-1} [\hat{F}_q] [R] \quad (\text{A61})$$

In summary, the steps are:

- Compute H_{xy} , H_{yy} , and H_{zy} in real space from the square brackets in Equation (A34).
- Compute the Fourier transforms $H_{xy,q}$, $H_{yy,q}$, and $H_{zy,q}$.
- Rotate the coordinate system obtain $H^{\hat{xy},q}$, $H^{\hat{yy},q}$, and $H^{\hat{zy},q}$.
- Calculate \hat{u}_q^T , using the matrix $[F_q]$ from Equation (A59).
- Revert the rotation to obtain u^T .
- Use u^T on the right-hand side in Equation (A32) to compute the populations traveling downward (which are h_4 , h_8 , h_{12} , h_{13} , and h_{18}).

An example of velocities at the top boundary obtained in this way is shown in **Figure A4**.

Acknowledgements

The authors thank John Sader for a helpful discussion at the beginning of this project. The authors appreciate input by Sunil Gopalakrishna, Gunther Brenner, and Hozan Ibrahim. This work was funded by the Deutsche Forschungsgemeinschaft under contract Jo278/23-1 (grant number 324062370).

Open access funding enabled and organized by Projekt DEAL.

Conflict of Interest

Advanced Wave Sensors S.L. is a company that designs, develops, builds, and markets research-grade and custom-made QCMD systems, sensors, associated fluidics, software, and electronics. I.R. is employed by, and owns stock in, AWSensors.

Data Availability Statement

The data that support the findings of this study are available from the corresponding author upon reasonable request.

Keywords

contact stiffness, lattice Boltzmann method, particle adsorption, QCM-D, roughness

Received: November 21, 2024
Revised: January 13, 2025
Published online: March 12, 2025

- C. Steinem, A. Janshoff *Piezoelectric Sensors*, Springer, Heidelberg, 2007.
- D. Johannsmann, A. Langhoff, C. Leppin, *Sensors* **2021**, 21, 3490.
- K. K. Kanazawa, J. G. Gordon, *Anal. Chem.* **1985**, 57, 1770.
- A. P. Borovikov, *Instrum. Exp. Tech.* **1976**, 19, 223.
- G. Sauerbrey, *Z. Phys.* **1959**, 155, 206.
- S. Liu, J. Kim, *JALA* **2009**, 14, 213.
- D. Johannsmann, A. Langhoff, C. Leppin, I. Reviakine, A. M. C. Maan, *Sensors* **2023**, 23.
- D. Johannsmann, I. Reviakine, *Nature Reviews Methods Primers* **2024**, 4, 63.
- C. A. Keller, B. Kasemo, *Biophys. J.* **1998**, 75, 1397.
- Z. Adamczyk, M. Sadowska, *Anal. Chem.* **2020**, 92, 3896.
- C. Grunewald, M. Schmutte, C. N. Noufele, C. Graf, T. Risse, *Anal. Chem.* **2015**, 87, 10642.
- L. Daikhin, E. Gileadi, G. Katz, V. Tsionsky, M. Urbakh, D. Zagidulin, *Anal. Chem.* **2002**, 74, 554.
- F. Eggers, T. Funck, *Journal of Physics E-Scientific Instruments* **1987**, 20, 523.
- D. Johannsmann, I. Reviakine, E. Rojas, M. Gallego, *Anal. Chem.* **2008**, 80, 8891.
- X. Xie, Y. Liu, Y. Ye, *IOP Conf. Ser. Mater. Sci. Eng.* **2020**, 892, 12072.
- A. Vázquez-Quesada, M. M. Schofield, A. Tsortos, P. Mateos-Gil, D. Milioni, E. Gizeli, R. Delgado-Buscalioni, *Phys. Rev. Applied* **2020**, 13, 064059.
- R. Delgado-Buscalioni, *Langmuir* **2024**, 40, 580.
- F. Balboa Usabiaga, R. Delgado-Buscalioni, B. E. Griffith, A. Donev, *Comput. Methods Appl. Mech. Eng.* **2014**, 269, 139.
- J. J. Gillissen, S. R. Tabaei, J. A. Jackman, N. J. Cho, *Analyst* **2017**, 2, 3370.

- [20] J. J. J. Gillissen, J. A. Jackman, S. R. Tabaei, N. J. Cho, *Anal. Chem.* **2018**, *90*, 2238.
- [21] P. Neumann, H. Bungartz, M. Mehl, T. Neckel, T. Weinzierl, *Commun. Comput. Phys.* **2012**, *12*, 65.
- [22] T. Krüger, H. Kusumaatmaja, A. Kuzmin, O. Shardt, G. Silva, E. M. Viggien, *The Lattice Boltzmann Method, Principles and Practice*, Springer, Berlin **2017**.
- [23] Y. Shi, J. E. Sader, *Phys. Rev. E* **2010**, *81*, 036706.
- [24] E. M. Viggien, *Philos. Trans. R. Soc. Math. Phys. Eng. Sci.* **2017**, *11*, 2246.
- [25] Ch 12: Sound Waves, In *The Lattice Boltzmann Method, Principles and Practice*, Springer, Berlin **2017**.
- [26] D. Johannsmann, G. Brenner, *Anal. Chem.* **2015**, *87*, 7476.
- [27] S. Gopalakrishna, A. Langhoff, G. Brenner, D. Johannsmann, *Anal. Chem.* **2021**, *93*, 10229.
- [28] D. Johannsmann, J. Petri, C. Leppin, A. Langhoff, H. Ibrahim, *Results Phys.* **2023**, *45*, 106219.
- [29] D. Johannsmann, C. Leppin, A. Langhoff, *Adv. Theor. Sims.* **2023**, *6*, 2300190.
- [30] A. J. C. Ladd, *J. Fluid Mechan.* **1994**, *271*, 285.
- [31] C. Sun, F. Perot, R. Zhang, D. M. Freed, H. Chen, *Commun. Comput. Phys.* **2013**, *13*, 757.
- [32] M. Rodahl, F. Hook, A. Krozer, P. Brzezinski, B. Kasemo, *Rev. Sci. Instrum.* **1995**, *66*, 36.
- [33] A. M. Leshansky, B. Y. Rubinstein, I. Fouxon, D. Johannsmann, M. Sadowska, Z. Adamczyk, *Anal. Chem.* **2024**, *96*, 10559.
- [34] S. J. Martin, G. C. Frye, A. J. Ricco, S. D. Senturia, *Anal. Chem.* **1993**, *65*, 2910.
- [35] E. Tellechea, D. Johannsmann, N. F. Steinmetz, R. P. Richter, I. Reviakine, *Langmuir* **2009**, *25*, 517784.
- [36] I. Reviakine, M. Gallego, D. Johannsmann, E. Tellechea, *J. Chem. Phys.* **2012**, *136*, 084702.
- [37] M. V. Voinova, M. Jonson, B. Kasemo, *Biosens. Bioelectron.* **2002**, *17*, 835.
- [38] M. Rubinstein, R. H. Colby *Polymer Physics*, Oxford University Press, Oxford, UK **2003**.
- [39] S. Hanke, J. Petri, D. Johannsmann, *Phys. Rev. E* **2013**, *88*, 032408.
- [40] B. Borovsky, A. Booth, E. Manlove, *Appl. Phys. Lett.* **2007**, *91*.
- [41] M. A. Cooper, F. N. Dultsev, T. Minson, V. P. Ostanin, C. Abell, D. Klenerman, *Nat. Biotechnol.* **2001**, *19*, 833.
- [42] M. Edvardsson, M. Rodahl, B. Kasemo, F. A Hook, *Anal. Chem.* **2005**, *77*, 61.
- [43] R. König, A. Langhoff, D. Johannsmann, *Phys. Rev. E* **2014**, *89*, 043016.
- [44] M. Bouzidi, M. Firdouss, P. Lallemand, *Phys. Fluids* **2001**, *13*, 3452.
- [45] P. L. Bhatnagar, E. P. Gross, M. Krook, *Phys. Rev.* **1954**, *94*, 511.
- [46] M. E. O'Neill, *Chem. Eng. Sci.* **1968**, *23*, 1293.
- [47] A. Tarnapolsky, V. Freger, *Anal. Chem.* **2018**, *90*, 13960.
- [48] H. Fischer, I. Polikarpov, A. F. Craievich, *Protein Sci.* **2004**, *13*, 2825.
- [49] D. Johannsmann, *Macromol. Chem. Phys.* **1999**, *200*, 501.
- [50] L. D. Landau, E. M. Lifshitz., In *Fluid Mechanics*, Pergamon Press, Oxford, UK, **1987**, p 89.
- [51] G. G. Stokes, *Trans. Cambr. Philos. Soc.* **1851**, *9*, 8.
- [52] G. Dolfo, J. Vigué, D. Lhuillier, *Phys. Rev. Fluids* **2021**, *6*, 104101.
- [53] M. Urbakh, L. Daikhin, *Phys. Rev. B* **1994**, *49*, 4866.
- [54] M. Urbakh, L. Daikhin, *Langmuir* **1994**, *10*, 2836.
- [55] A. Bund, O. Schneider, V. Dehnke, *Phys. Chem. Chem. Phys.* **2002**, *4*, 3552.
- [56] I. Fouxon, B. Y. Rubinstein, A. M. Leshansky, *Phys. Rev. Fluids* **2023**, *8*, 054104.
- [57] A. Logg, K.-A. Mardal, G. N. Wells (Eds.), *Automated Solution of Differential Equations by the Finite Element Method*, The FEniCS Book Springer, Berlin/Heidelberg **2012**.
- [58] K. Selim, A. Logg, M. G. Larson, *Comput. Methods Appl. Mechan. Eng.* **2012**, *209–212*, 54.
- [59] P. Sinha, D. Roshini, V. Dao, B. M. Abraham, J. K. Singh, *Trans. Indian Natl. Acad. Eng.* **2023**, *8*, 7.
- [60] S. L. Brunton, J. L. Proctor, J. N. Kutz, *Proc. Natl. Acad. Sci. USA* **2016**, *113*, 3932.
- [61] R. Marcinkevičs, J. E. Vogt, *WIREs Data Mining Knowledge Discov.* **2023**, *13*, e1493.
- [62] V. Vanoppen, D. Johannsmann, X. Hou, J. Sjölund, P. Broqvist, E. J. Berg, *Adv. Sensor Res.* **2024**, *n/a*, 2400025.
- [63] V. L. Popov *Contact Mechanics and Friction: Physical Principles and Applications*, Springer, Berlin **2010**.
- [64] C. Dominik, A. Tielens, *Philos. Mag. A* **1995**, *72*, 783.
- [65] J. N. Israelachvili *Intermolecular and Surface Forces*, Elsevier, Cham **2011**.
- [66] M. Heuberger, C. Drummond, J. Israelachvili, *J. Phys. Chem. B* **1998**, *2*, 5038.
- [67] J. Klein, Y. Kamiyama, H. Yoshizawa, J. N. Israelachvili, G. H. Fredrickson, P. Pincus, L. J. Fetters, *Macromolecules* **1993**, *26*, 5552.
- [68] S. Berg, M. Ruths, D. Johannsmann, *Phys. Rev. E* **2002**, *65*, 026119.
- [69] S. Berg, M. Ruths, D. Johannsmann, *Rev. Sci. Instrum.* **2003**, *74*, 3845.
- [70] N. Shpigel, M. D. Levi, S. Sigalov, O. Girshevitz, D. Aurbach, L. Daikhin, P. Pikra, M. Marandi, A. Jänes, E. Lust, N. Jäckel, V. Presser, *Nat. Mater.* **2016**, *15*, 570.
- [71] A. Langhoff, D. Johannsmann, *Phys. Rev. E* **2013**, *88*, 013001.
- [72] I. Fouxon, B. Rubinstein, O. Weinstein, A. Leshansky, *Phys. Rev. Lett.* **2020**, *125*, 144501.
- [73] L. Chen, H. W. Zhang, L. Y. Liang, Z. Liu, Y. Qi, P. Lu, J. Chen, L. Q. Chen, *J. Power Sources* **2015**, *300*, 8.